Lawrence Radiation Laboratory
UNIVERSITY OF CALIFORNIA
LIVERMORE

UCRL-50482

PHENOMENOLOGY AND CONTAINMENT
OF UNDERGROUND NUCLEAR EXPLOSIONS

Lawrence S. Germain

J. S. Kahn

November 1968

DTIC QUALITY INSPECTED 4

20000908 184

Contents

PHENOMENOLOGY AND CONTAINMENT
OF UNDERGROUND NUCLEAR EXPLOSIONS

Introduction

This document will deal with some aspects of the phenomenology of underground nuclear explosions. It is divided into four general sections.

First, we shall examine the rather extensive history of routine underground explosions and note that, from a pragmatic point of view, a nuclear explosion can be contained by putting it underground. Those few cases where some radioactivity was released will be examined to see if they can be categorized or if there were extenuating circumstances.

Second, we shall describe the calculation of early-time phenomenology—the interactions between a nuclear explosion and the media surrounding it during the first few tenths of a second after the explosion. We shall attempt to substantiate these calculations by showing how well they agree with actual measurements.

Third, we will present a parallel discussion of the calculation of late-time phenomenology and the verification of these calculations by field observations.

Fourth, we shall address the question of how containment is affected by geological features such as faults and joints.

Before going into our detailed discussion, let us describe in general the phenomena involved in an underground nuclear explosion. Picture a 10-kiloton (kt) source buried 750 ft below the desert surface in Yucca Flat. When the nuclear detonation occurs, this large amount of energy is produced in a very short time, perhaps about 10^{-7} sec. The material in the nuclear device is not only instantly vaporized but also raised to a temperature of several million degrees Kelvin. A strong shock moves from this hot, high-pressure region, vaporizing some of the surrounding earth. At this point, a cavity has been formed, having a radius of about 15 ft and containing rock vapor at a pressure of about 1 megabar (Mbar: one-million atmospheres). The cavity continues to expand for about 100 milliseconds (msec), until its pressure drops to a value about equal to the ambient hydrostatic overpressure (ρgh). For 750 ft of alluvium this would be about 50 bars. The cavity now has a radius of about 100 ft.

While the cavity is growing, the main shock from the explosion is moving towards the ground surface. It arrives there about 100 msec after the explosion and causes the surface to rise momentarily by about a foot; then the shock is reflected back as a rarefaction. The passage of the main shock causes failure

in much of the material between the shot point and ground surface. The failure may be either brittle or plastic, depending on the stress conditions and the properties of the material.

The foregoing describes what we shall term early-time phenomenology; late-time phenomenology commences after the cavity has been stabilized and shocks and elastic waves have been dissipated. At about this time the rock gases condense, leaving water vapor as the most important component of the cavity gases. The cavity gases cool by simple Newtonian heat transfer to the cavity wall, and consequently the cavity pressure drops. Continued cooling leads to condensation of some of the more condensable cavity gases (such as water). The transfer of heat from the gases to the surrounding rock establishes a high thermal gradient in the cavity wall, resulting in cracking and flaking of the cavity surface. This in turn enhances the cooling rate by mixing earth into the cavity gases.

Ultimately, after a period which may be minutes or may be hours, as a result of both decrease of cavity pressure and cracking in the cavity wall, the cavity can no longer support itself and collapses. The collapse propagates upward in a few seconds through the material which has been cracked by the explosion and forms a chimney of rubble. The rubble quenches the remaining condensable gases in the cavity. Figure 1 is a photograph of a cavity that did not completely collapse. It shows how a typical cavity would look as

Fig. 1. Cavity formed by an underground nuclear explosion. The man standing on the rubble pile (arrow) indicates the scale.
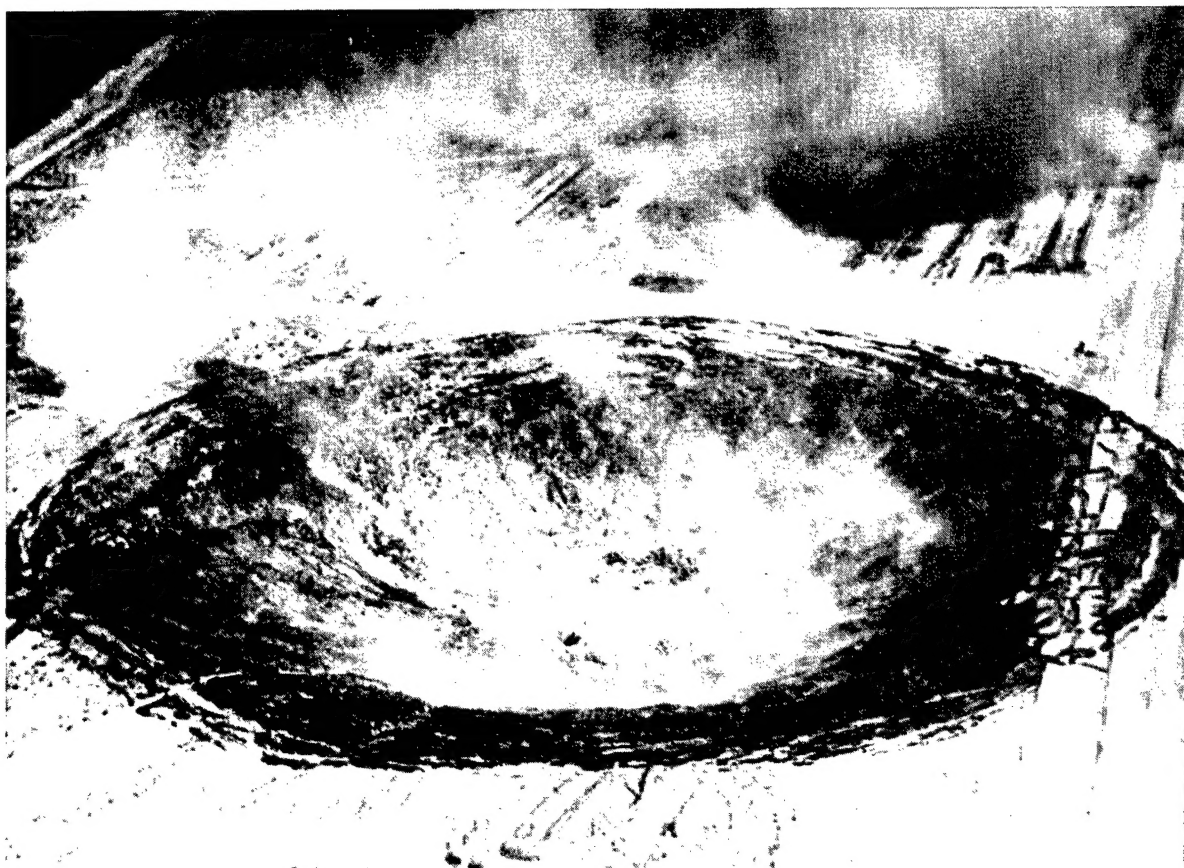
Figure 2.   Formation of a subsidence crater.

collapse begins, after some rubble has fallen from the roof to the floor.   If the chimney does not encounter rock which is strong enough to support a roof span of about one cavity diameter, as is frequently the case when alluvium is the emplacement material, collapse will continue to propagate upward and will reach the surface and form a crater.   A typical subsidence crater, at the moment of formation, is shown in Fig. 2.   For our sample shot we would expect a crater about 200 ft in radius and perhaps 50 ft deep.

The remaining noncondensable cavity gases, now at a pressure of only a few pounds per square inch (psi), are trapped in the rubble and can now reach the surface only by a long and tortuous path.

Past Experience

We have chosen to examine the population of nuclear-test shots having these two properties in common:

1. They were all fired in vertical holes without line-of-sight pipes or other direct communication with the surface.

2. They were all fired after the resumption of nuclear testing in 1961.

Table I summarizes this population by dividing it into intervals of yield and intervals of scaled depth of burial. Within each category, the total number of events and the number of events in which there was significant leakage are indicated. "Significant leakage" is defined as a total release of radioactivity of more than 100 curies (Ci).

Scaled depth of burial is the actual depth divided by the cube root of the yield; it is a convenient number of use because, assuming that the energy from a shot is dissipated uniformly in the volume around the shot point (hence the cube-root factor), the pressure arriving at the surface will be the same for all shots having the same scaled depth of burial in the same material. Consequently, most rules of thumb concerning successful containment are expressed in terms of scaled depth of burial.

As stated above, we set the dividing line between successful containment and significant leakage, in terms of total release, at 100 Ci. Expressing total release in curies (1 Ci = 3.7×10^{10} disintegrations per second) is not completely unambiguous, since the release of a given number of atoms of a given species will produce different numbers of disintegrations per second, depending on the time of detection. We have therefore adopted the practice of converting all measurements to the number of disintegrations which would be given at 12 hr after release time (R). In essence, our quoted total release is that activity which would be given if one could capture all of the released material in one place at R + 12 hr. The seemingly arbitrary limit of 100 Ci was chosen because, in general, the release

Table I. Total population of events, categorized by yield (W) and scaled depth of burial (SDOB).

| (ft/kt$^{1/3}$) | Low yield | | | | Low-intermediate yield | | Intermediate yield | | High yield | | Totals | |
| | W $\leq$ 5 kt | | 5 < W $\leq$ 20 kt | | 20 < W $\leq$ 200 kt | | 200 < W $\leq$ 1000 kt | | W > 1000 kt | | | |
	Events	Leakage	Events	Leakage	Events	Leakage	Events	Leakage	Events	Leakage	Events	Leakage
$\leq$ 350	3	1	8	1	3	0	0	—	0	—	14	2
> 350 $\leq$ 400	2	1	16	1	11	1	4	0	1	0	34	3
> 400 $\leq$ 450	14	1	16	0	12	0	1	0	0	—	43	1
> 450 $\leq$ 500	20	2	9	0	9	0	0	—	0	—	38	2
> 500 $\leq$ 600	28	2	4	0	5	0	0	—	0	—	37	2
> 600 $\leq$ 800	15	0	8	0	1	0	0	—	0	—	24	0
Totals	82	7	61	2	41	1	5	0	1	0	190	10

must go well above 100 Ci before one has to worry about off-site detection of the activity.

Table I indicates that there was significant leakage in 10 events. The amount of radioactivity that was leaked in these events varied from 200 Ci up to 10^5 or 10^6 Ci. Three events vented through ground fissures within the first minute after shot time. Of these three, only one had a scaled depth of burial greater than 350 ft/kt$^{1/3}$. In general, the others did not leak radioactivity until after collapse. A detailed examination of the 10 events that leaked reveals that five of them were atypical in that they were fired in dolomite (a carbonate rock), were located very close to a fault, or involved unusual downhole geometries. The other five were all in the low or low-intermediate yield range.

The one event of intermediate yield that showed some leakage was fired in water-saturated dolomite. In such a medium, one would expect that the shot would produce a large quantity of noncondensable CO_2 gas, which would not be present in any shot of the same yield in tuff or alluvium. It is reasonable to assume that the noncondensable CO_2 eventually diffused to the surface, bringing with it noncondensable fission products. Our experience with detonations in carbonate rock is limited, but it suggests that radioactivity is more likely to be released from a detonation in carbonate rock than from detonations in other formations.

The picture that emerges from these observations is one of some concern for seepage of radioactive gases from low-yield shots but remarkable success with containment in the higher-yield shots. The seepage from low-yield shots has seldom posed a serious problem and indeed has seldom been detectable off site. Our success in containing high-yield events is encouraging.

Early-Time Phenomenology

CALCULATIONAL METHODS

In any underground nuclear explosion, the shock front that propagates from the shot point carries with it energy from the explosion, and it distributes this energy by doing work on the surrounding material. In the process, the material undergoes changes in both its physical and mechanical states. If enough energy is deposited in the material, the material will vaporize or melt, changing its physical state, or it may crush or crack.

Special computer codes have recently been developed for predicting the close-in phenomena of underground nuclear explosions; they are based on the laws of physics and the knowledge of the properties of the materials in which the detonations occur. As a consequence, a better understanding of experimental observations and measurements has evolved.

A spherically symmetric, Lagrangian, hydrodynamic-elastic-plastic code called SOC is now being used in making these calculations (Ref. 1). A similar code in

two dimensions, TENSOR, is also available (Ref. 2). The general calculational procedure in these codes is described below.

Procedure (Ref. 3)

Clearly, the rock vapor causes stresses in the surrounding medium. The equation of motion provides a functional relationship between the applied stress field and the resulting acceleration of each point in the medium. Accelerations, when allowed to act over a small time increment, Δt, produce new velocities; velocities produce displacements, displacements produce strains, and strains produce a new stress field. Time is advanced by Δt, and the cycle is repeated. The time increment is determined by an independent stability condition which requires the increment to be smaller than the time necessary for a compressional wave to travel across the smallest zone.

Two areas in the above loop need further discussion: (1) the manner in which the stress field produces accelerations, and (2) the manner in which the strain field is coupled to the stress field through the equation of state of the medium. We limit the discussion here to spherical symmetry, and we attempt to interpret the equation of motion and medium behavior in a general way.

The fundamental equations of continuum mechanics (conservation of mass, linear momentum, and angular momentum) combine to produce the Eulerian equation of motion:

$$\rho \dot{u}_R = - \left(\frac{\partial P}{\partial R} + \frac{4}{3} \frac{\partial K_s}{\partial R} + 4 \frac{K_s}{R} \right) \quad (1)$$

and the stress tensor in the spherically symmetric coordinate system is written as the sum of an isotropic tensor and a deviatoric tensor:

$$
\begin{bmatrix} T_{RR} & 0 & 0 \\ 0 & T_{\theta\theta} & 0 \\ 0 & 0 & T_{\phi\phi} \end{bmatrix} \quad (T_{\theta\theta} = T_{\phi\phi})
$$

$$
= \begin{bmatrix} -P & 0 & 0 \\ 0 & -P & 0 \\ 0 & 0 & -P \end{bmatrix} \quad (2)
$$

$$
+ \begin{bmatrix} \frac{4}{3} K_s & 0 & 0 \\ 0 & \frac{2}{3} K_s & 0 \\ 0 & 0 & \frac{2}{3} K_s \end{bmatrix}
$$

where

ρ = density,

$\dot{u}_R$ = particle acceleration,

R = space variable (radius),

P = mean stress,

$T_{RR}, T_{\theta\theta}, T_{\phi\phi}$ = radial and tangential stresses, and

K_s = stress deviator.

We see from Eq. (2) that

$$P = -\frac{1}{3} (T_{RR} + T_{\theta\theta} + T_{\phi\phi})$$

and

$$K_s = \frac{T_{\theta\theta} - T_{RR}}{2} . \quad (3)$$

Equation (1) shows that the two stresses causing the acceleration are P and K_s. When this equation is differenced we obtain a functional relation between stress gradients and the acceleration of a point in the medium. The forces that are driving the stress wave, P and K_s, are invariant tensor quantities in the one-dimensional formulation.

The first invariant of the stress tensor, I_1, is given by

$$I_1 = T_{11} + T_{22} + T_{33}.$$

Thus

$$P = -\frac{1}{3} I_1 \quad \text{and}$$

$$K_s = \frac{1}{2} \sqrt{3 I_{2D}} ,$$

where I_{2D} is the second invariant of the deviatoric stress tensor.

Initial conditions for such a problem involve specifying the properties of the vaporized rock. Equilibrium equations of state have been developed for various natural materials in which underground nuclear and high-explosive detonations have occurred. A set of assumptions was made to obtain the gas equation of state (Ref. 4). One of these was that the materials behave like a perfect gas of molecules and ions below about 3 electron volts (eV) and like a perfect gas of atoms, electrons, and nuclei above 3 eV. At liquid and solid densities, the experimentally determined Hugoniot equation of state was used, and the state points were obtained from interpolation between the Hugoniot measurements and points at about 50 eV.

The adiabatic expansion of a gas is calculated using another set of assumptions, namely, that the required increase in enthalpy to cause vaporization— 2800 calories per gram (cal/g) for a silicate rock—is equal to the "waste heat" when the Hugoniot is assumed to be the unloading curve (see Fig. 3). The initial pressure of the gas vapor is equal to the pressure of vaporization, and its initial density is equal to the bulk density of the material.

A series of calculations (Ref. 4) has shown that the radius of vaporization, R_V, depends on the yield, W, and the energy of vaporization, E_V:

$$R_V = 1.524 \, W^{1/3} \, E_V^{-0.256},$$

where R_V is in meters, W is in kt, and E_V is in 10^{12} ergs per cubic centimeter (cc).

E_V is related to the pressure of vaporization and specific volume by:
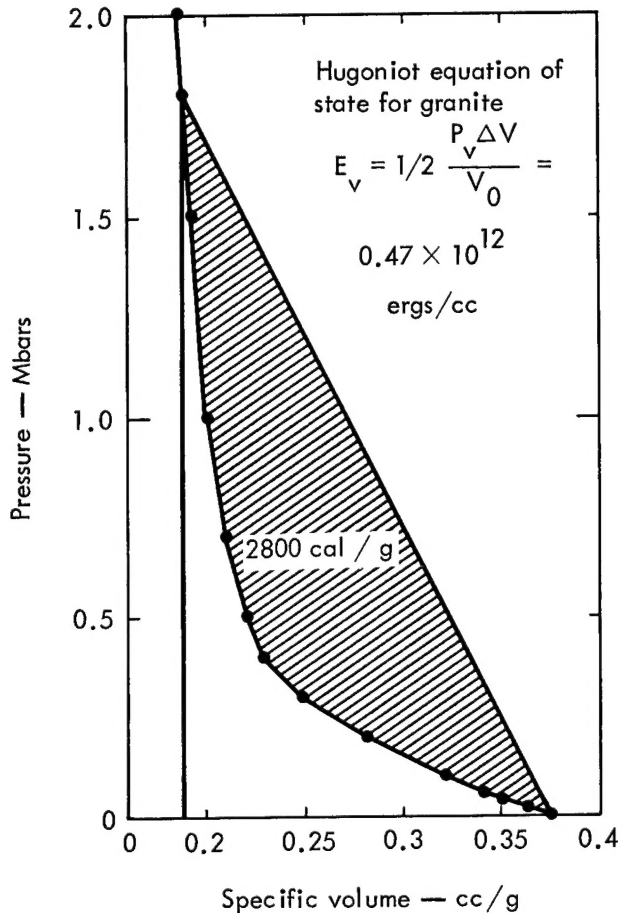
$$E_V = \frac{1}{2} \frac{P_V \Delta V}{V_0} ,$$

Fig. 3. Shock Hugoniot for granite (shaded area represents "waste heat").

where

P_V = pressure of vaporization,

ΔV = specific volume change, and

V_0 = initial specific volume.

The energy density in the gas is independent of the yield, since R_V^3 is proportional to W. The internal energy of this gas in cal/g is given by

$$E_0 = \frac{10^{12}}{\frac{4}{3}\pi \rho_0 \left(R_V^{1\ kt}\right)},$$

where

$R_V^{1\ kt} = 1.524\ E_V^{-0.256}$, and

ρ_0 = bulk density of the material.

The rock gas is then allowed to expand adiabatically from the point defined by ρ_0, E_0, and P_V according to the equilibrium equation of state derived as described above.

Results

Histories of the effects of 10-kt underground nuclear explosions on the surrounding media, as calculated by the SOC code, are shown in Figs. 4 and 5. In Fig. 4 the explosion is at a depth of 400 m, while in Fig. 5 it is at a depth of only 150 m. The two histories are significantly different. At a depth of burial of 400 m, the cavity growth is unaffected by the rarefaction from the surface, since it is so weak as to be imperceptible by the time it has reached the cavity. However, at a depth of burial of 150 m, the returning rarefaction allows renewed growth of the cavity by reducing the ambient pressure below that of the cavity.

The ability of the rarefaction from the surface to affect the cavity has been called the "gas-acceleration" phase of cavity growth. This gas-acceleration phase occurs if the surface is close enough to the explosion point to affect cavity growth. The expanding cavity can, in effect, sense the direction of the free surface and expand preferentially in that direction. When this occurs, one might have serious questions about the adequacy of containment. If, however, the gas-acceleration phase does not occur, the explosion is essentially in an infinite medium and is unaffected by the free surface. For these reasons we feel that the absence of the gas acceleration phase in the result of a calculation is a good physical criterion for the preclusion of dynamic venting.

A second difference between Figs. 4 and 5 is the absence of the elastic region at the 150-m depth of burial. In essence, at this depth one could expect the rock to fail by some mechanism at all points between the shot point and the surface.

Rock in this region can fail in a number of ways. There is a region immediately outside the cavity in which the temperature exceeds the melting point but not the vaporization point of the rock. Thus a relatively thin region of melt is produced. (This region is too thin to be conveniently shown in the figures.) Outside the melt zone there is a region where the material fails under compressive load with the passage of the shock. This is the region labeled "compressive failure" in the figures. However, the failure mechanism may be either plastic flow (ductile failure) or fracture (brittle failure). In the region labeled "compressive failure," if brittle failure occurs the cracks will be in the direction of greatest compressive stress, i.e., radial, or at some shear angle to the
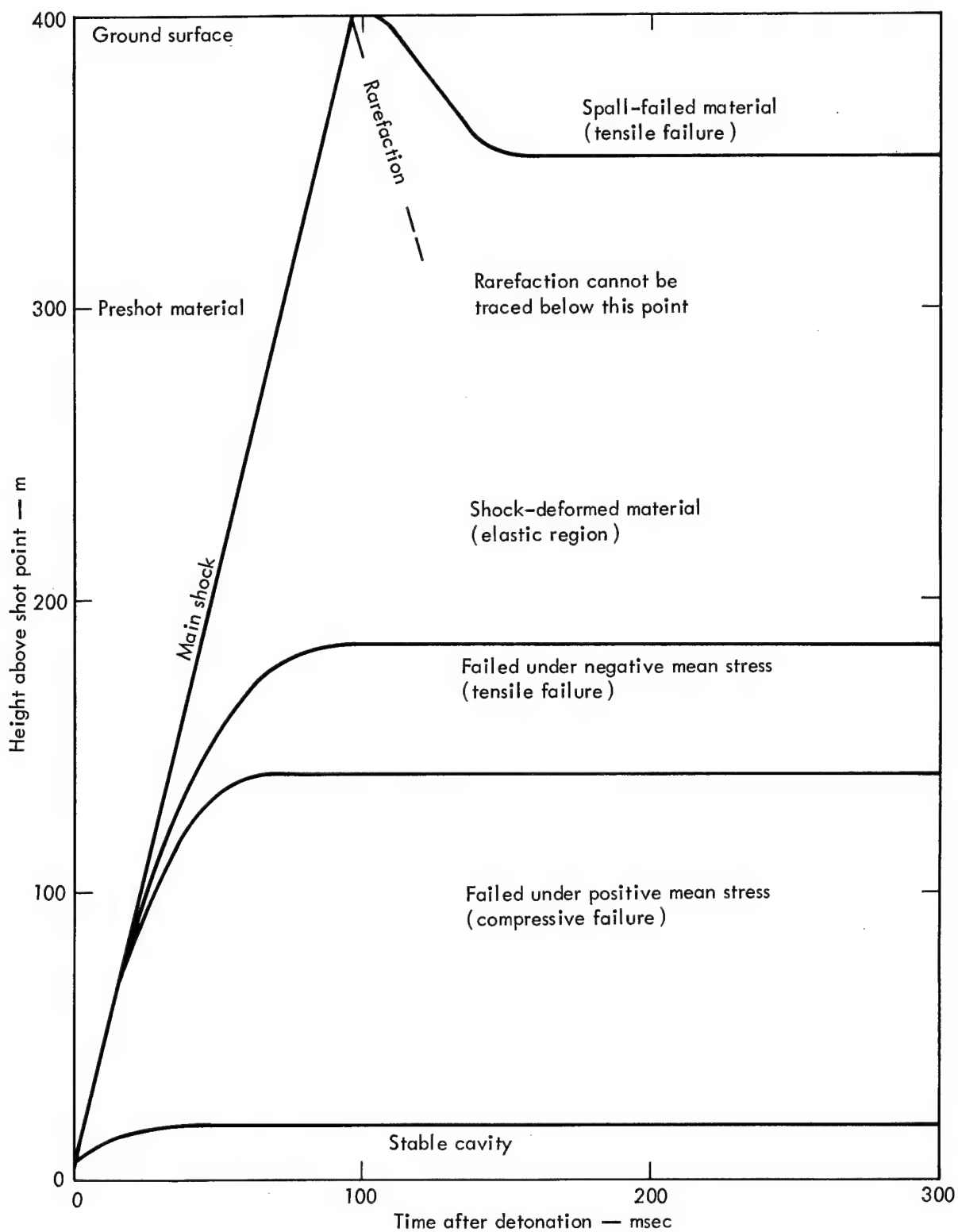
Fig. 4. Calculated effects of a deeply buried 10-kt nuclear explosion on the surrounding medium. Depth: 400 m; medium: Lewis shale (derived from Ref. 5).
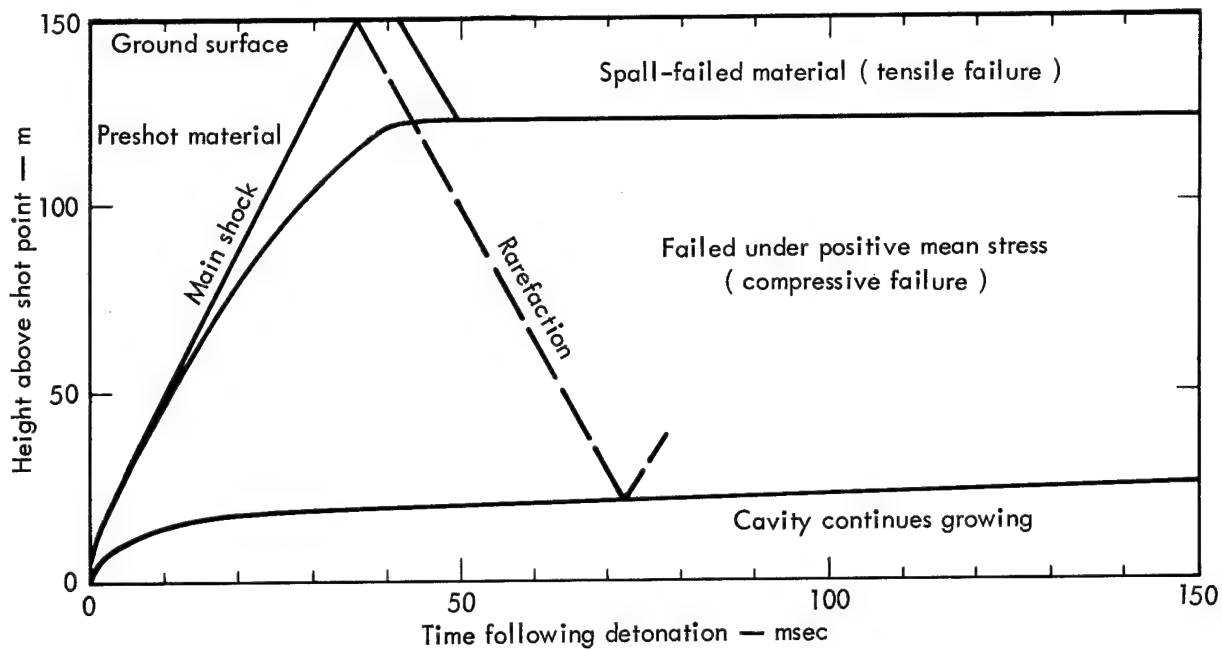
Fig. 5. Calculated effects of a near-surface 10-kt nuclear explosion on the surrounding medium. Depth: 150 m; medium: Lewis shale (derived from Ref. 5).

radius. Upon unloading by the following rarefaction, annular cracks will also be produced. Beyond the zone of compressive cracking is a region where a shock stress is not large enough to cause compressive failure, but tensile cracking is produced in the unloading phase. Again, these cracks are annular. This region is labeled in Fig. 4 as "Failed under negative mean stress (tensile failure)." A slightly different form of tensile cracking is produced near the surface, where the rarefaction reflected from the surface will produce a tension. The resulting tensile failure is called spall and is so labeled in the figures.

To calculate the extent of fracturing produced by the source, one must know the "strength" of the medium as a function of the state of stress. A direct approach is to plot the octohedral shear stress, which is equal to $(2I_{2D}/3)^{1/2}$, versus the mean stress, Pm, which is equal to $-I_1/3$. The results of various destructive tests (compression, extension, and hollow torsion) are shown for dolomite in Fig. 6. The plot clearly does not give a consistent failure surface when the test type is changed.

However, it has been found (see Fig. 7) that a consistent failure surface results if we define "strength" as a function, Y, as follows (Ref. 6):

$$Y = \frac{3}{4}\left[(3I_{2D})^{1/2} + \frac{I_3}{|I_3|}\left(\frac{|I_{3D}|}{2}\right)^{1/3}\right].$$

To review the various stress invariants let us write a general stress tensor (Ref. 7):

$$\begin{bmatrix} T_{11} & T_{12} & T_{13} \\ T_{21} & T_{22} & T_{23} \\ T_{31} & T_{32} & T_{33} \end{bmatrix} \qquad \left(T_{ij} = T_{ji}\right),$$
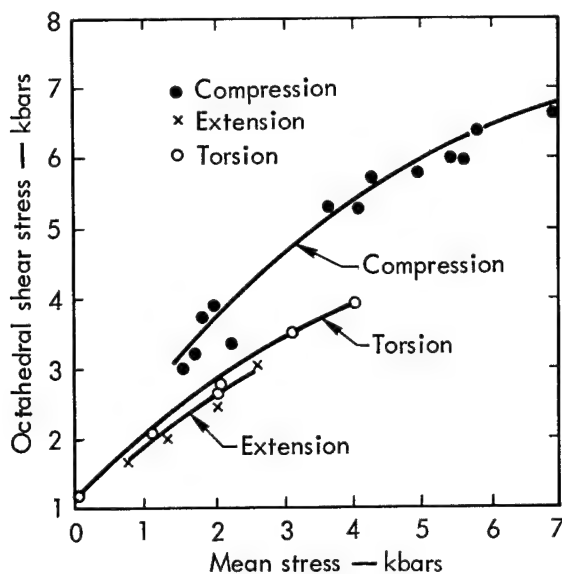
-10-

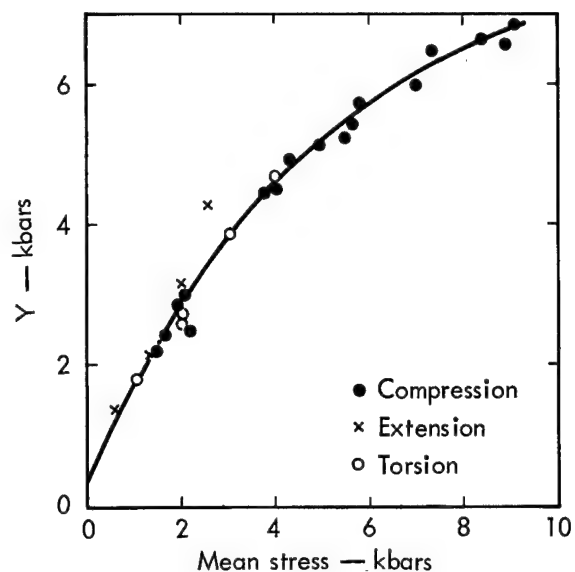Fig. 6. Octahedral shear stress versus mean stress for dolomite.

Fig. 7. Y versus mean stress for dolomite.

and write the stress deviators

$$T_1 = P_m + T_{11},$$
$$T_2 = P_m + T_{22},$$
$$T_3 = P_m + T_{33}.$$

then

$$I_3 = T_{11} T_{22} T_{33} + 2T_{12} T_{33} T_{31}$$
$$- T_{11} T_{23}^2 - T_{22} T_{31}^2 - T_{33} T_{12}^2,$$

$$I_{2D} = T_1 T_2 + T_2 T_3 + T_3 T_1 - T_{12}^2 - T_{31}^2,$$

$$I_{3D} = T_1 T_2 T_3 + 2T_{11} T_{23} T_{31} - T_1 T_{23}^2$$
$$- T_2 T_{31}^2 - T_3 T_{12}^2.$$

One should by no means assume that rock failure at all levels between the shot point and the surface implies the presence of an easy path by which radioactivity can reach the surface, thus causing delayed seepage. On the contrary, both field experience and calculations tell us that the time required for gas to diffuse through these cracks under the driving force of cavity pressure is long compared to the time it takes for cavity pressure to decay. This will be discussed in more detail later (p. 32).

The onset of the gas-acceleration phase of cavity growth can be determined by inspecting the value of the cavity radius as a function of yield (Fig. 8). At depths where there is no gas-acceleration phase, the cavity radius increases as $W^{1/3}$. There comes a point, however, where cavity radius begins to increase rapidly with further increase of yield; this rapid increase indicates the onset of gas acceleration. An estimate of the point at which each curve in Fig. 8 deviates from linear when plotted against yield gives a criterion for depth of burial by the gas-acceleration model in Lewis shale (Fig. 9). When compared with current
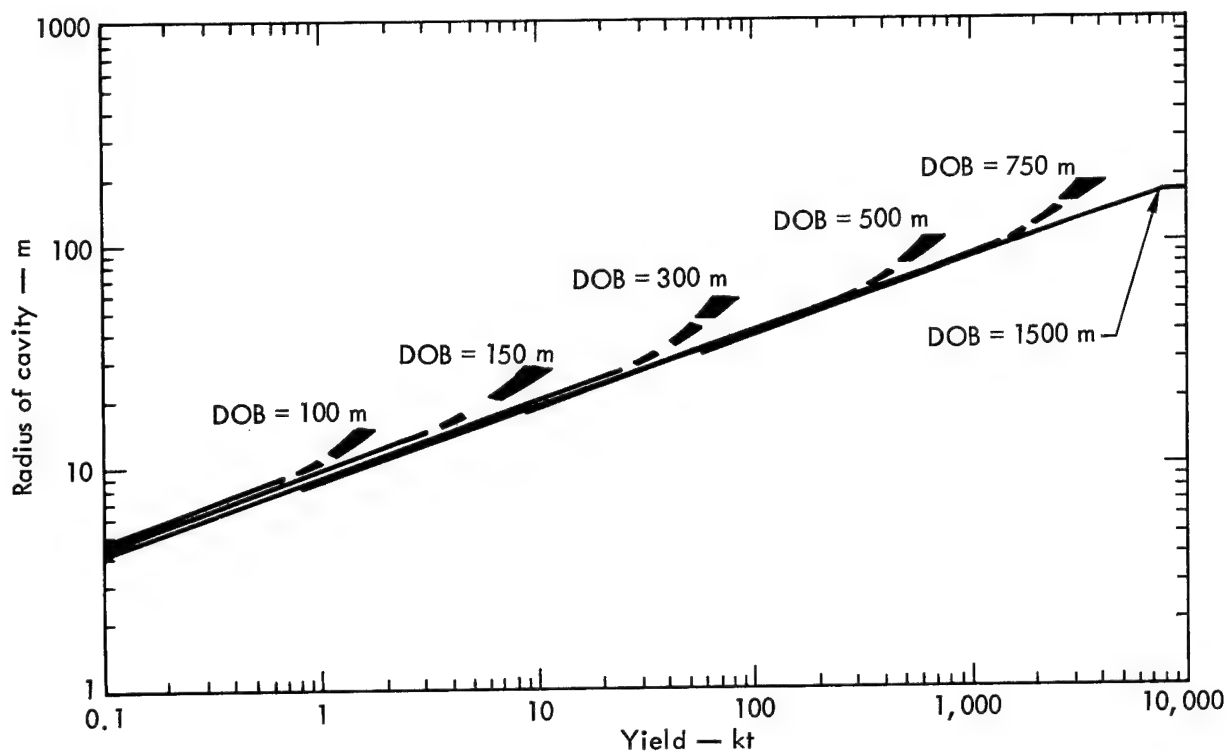
Fig. 8. Radius of cavity versus yield at various depths of burial (DOB); SOC model
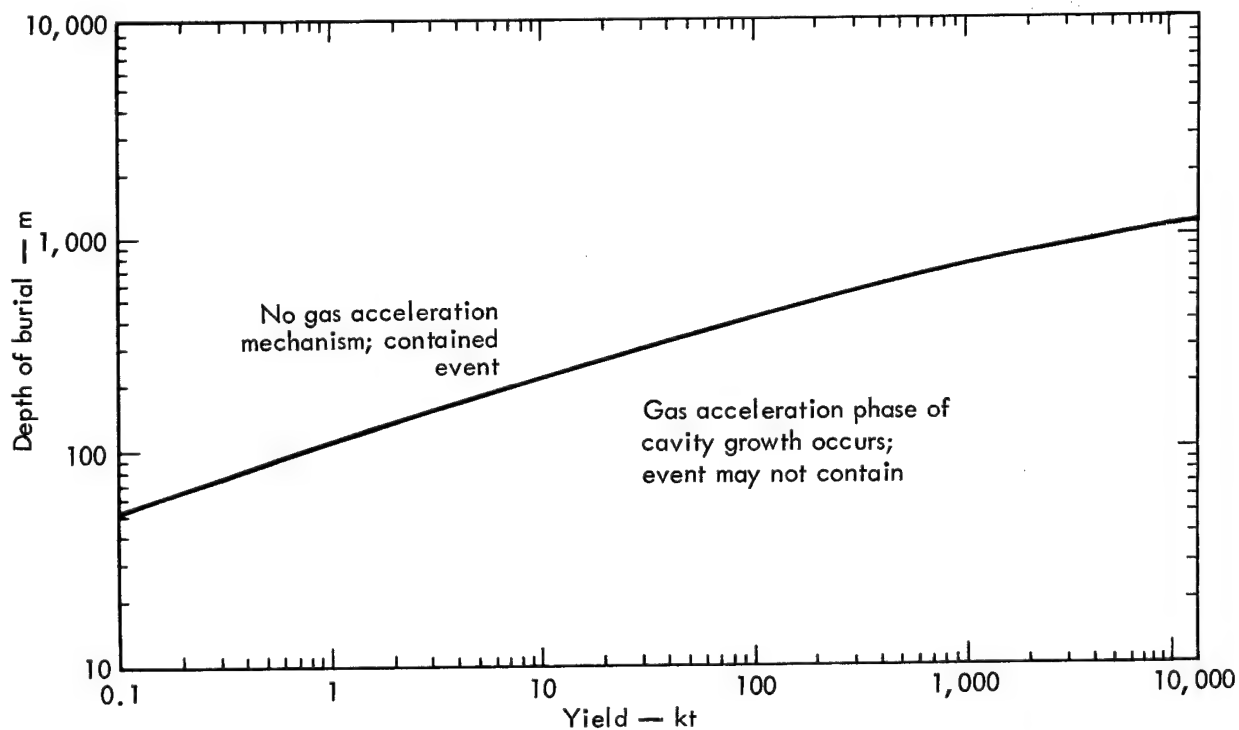study in Lewis shale   (Ref. 5).

Fig. 9. Burial criteria (gas acceleration in Lewis shale) (Ref. 5).

practice the criterion is seen to be consistent in the yield region where most of our experience lies (1 to 50 kt), and the comparison indicates that our current practice is quite conservative in the higher yield range.

Using a criterion like gas acceleration instead of a rule of thumb places the subject of containment on a firmer technical footing, but it also introduces complications. The gas-acceleration criterion is, like containment itself, clearly dependent on material properties, since it arose from a calculation which involved material properties. The extent of this material dependence is suggested in Figs. 10 and 11. Figure 10 shows cavity radii and failure radii for the same yield and depth of burial in several different media. Figure 11 shows the depth-of-burial criterion derived from gas acceleration for several different media.

The rock property which probably has the greatest effect on the presence or absence of the gas acceleration phase is compactability, the nonreversible compression caused by elimination of void spaces. Since this compression is done under considerable shock pressure, much energy in the form of $P \Delta V$ work is locally deposited as internal energy and thus removed from the energy available to the hydrodynamic shock. Removal of energy from the shock will in turn remove energy from the returning rarefaction and thus inhibit the gas-acceleration phase. Compactability is strongly related to the porosity, ratio of void volume to total volume, and degree of saturation (how much of the void volume is full of water) of the medium. At present these quantities

are difficult to determine unless one obtains samples of the media in the neighborhood of the explosion. However, one can get some help in evaluating compactability from more easily measured properties, such as density and sonic velocity.

Shock velocity within the medium is clearly important since it determines the interval between the explosion and the arrival back at the cavity of a signal reflected from the surface. The shorter this interval the more probable is a gas-acceleration phase, because one has caught the cavity in an earlier stage of its growth.

The exact shape of the PV curve of the material is also important. If the PV curve shows considerable curvature (refer to Fig. 3), the velocity of the rarefaction following the shock (given by the local slope at the appropriate value of P) will be higher than that of the shock itself (given by the average slope from $P = 0$ up to P). Thus the following rarefaction will catch up to the shock and weaken it. Again, any weakening of the shock will weaken the gas-acceleration phase of cavity growth.

COMPARISON OF CALCULATIONS AND EXPERIMENTS

There have been many experiments in which nuclear phenomenological effects have been both predicted and measured. Typical examples in different rock materials are the Piledriver, Salmon, Gasbuggy, and Cabriolet Events. Cabriolet was a cratering experiment, and the other three were contained underground events.

Piledriver Event

Piledriver was an approximately 60-kt explosion in granite at the Nevada Test Site (NTS). The mechanical properties of
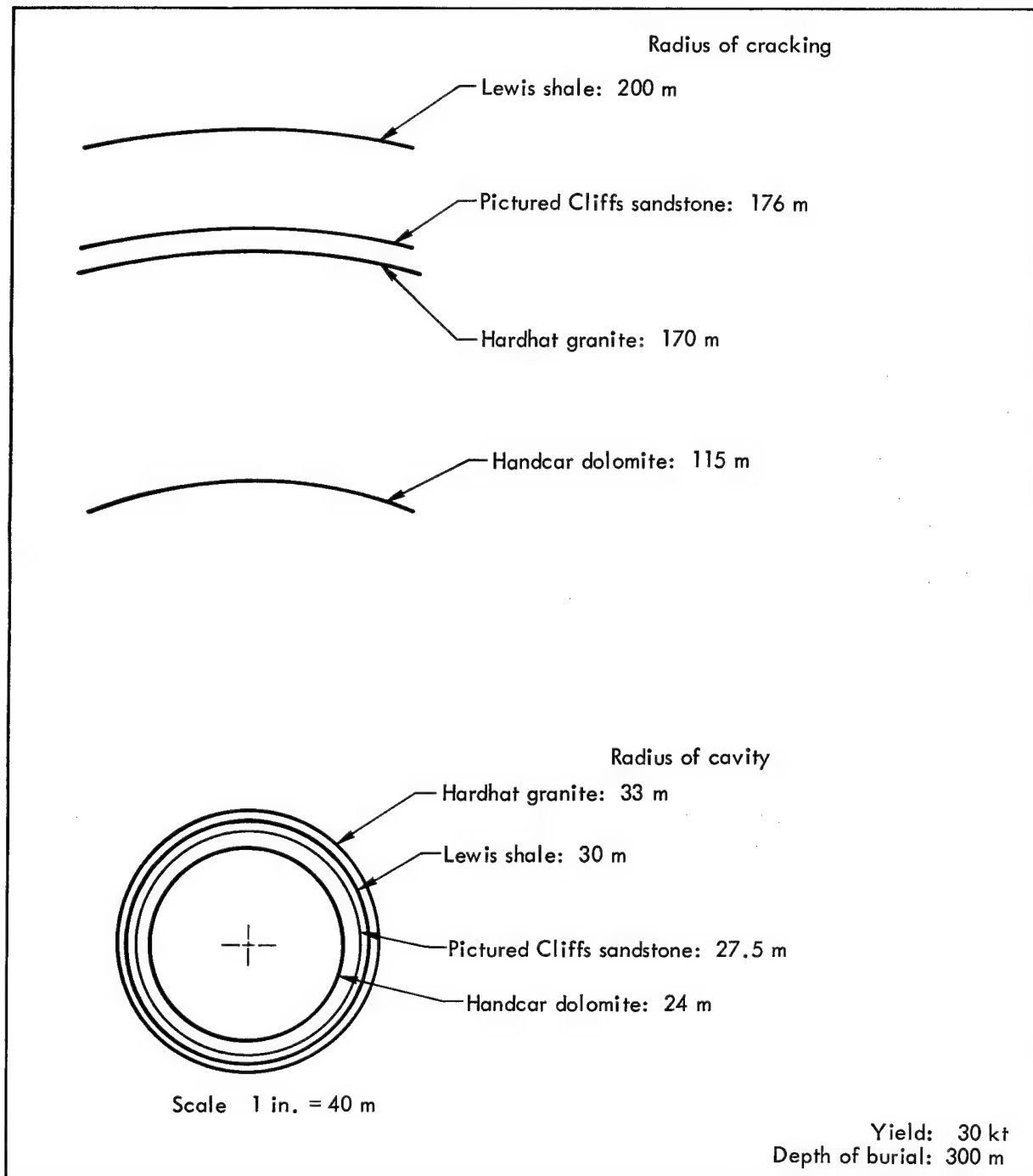
Fig. 10. Radius of compressive cracking and cavity as a function of medium: calculation model study.
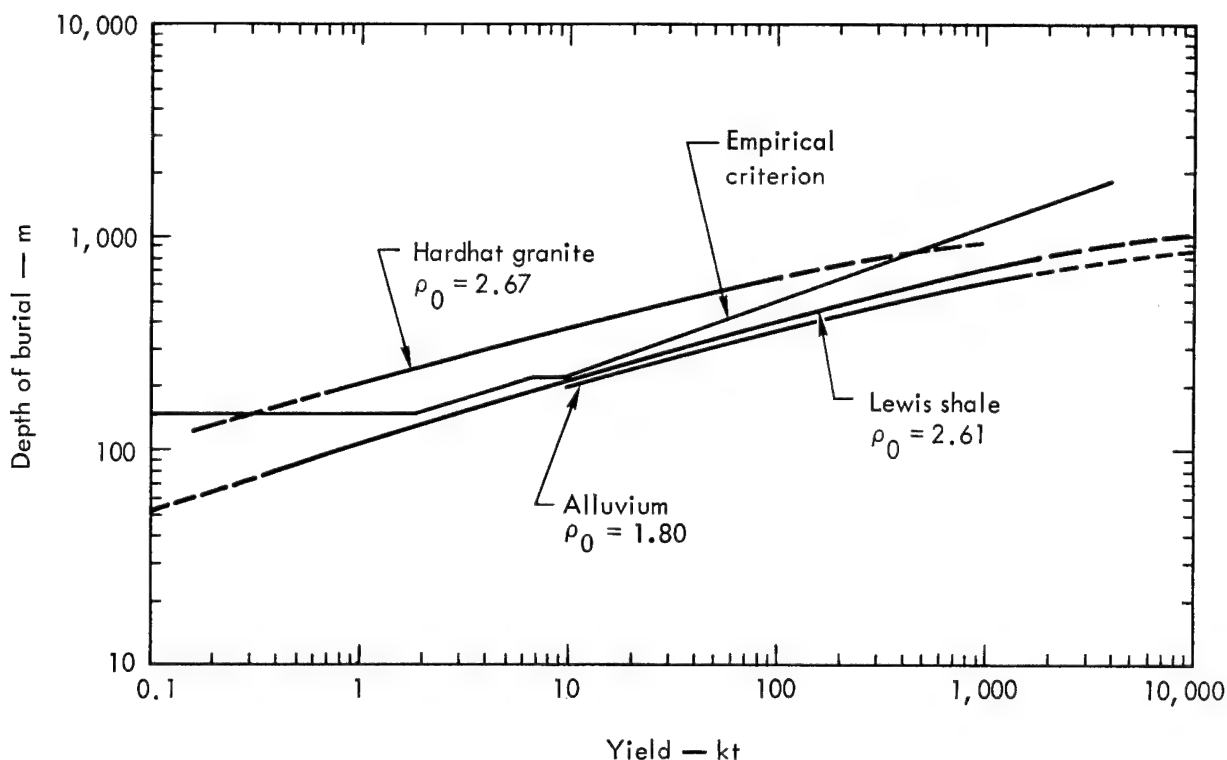
Fig. 11. Depth-versus-yield criterion for gas acceleration as a function of medium.

this granite had been previously determined for the Hardhat experiment, and those equation-of-state (EOS) data served as the EOS data for the analysis of Piledriver.

Calculations (Ref. 8)

Two SOC code runs were made, one vertically with the free surface 463 m above the device, the other horizontally with a constant overburden of 463 m and no free surface. These calculations are summarized in Fig. 12. Here a plot of cavity radius as a function of time demonstrates the role that the free surface plays in the physics of cavity formation. The two SOC runs are identical until the rarefaction arrives back from the free surface to the growing cavity. This wave is large enough to cause significant changes

in cavity growth rate, as evidenced by the slope change for the vertical SOC run at about 2×10^2 msec. This phenomenon is recognized as the gas-acceleration phase of cavity growth, which has been previously described. In spite of the fact that the vertical calculations indicated gas acceleration, the explosion contained.

The calculated cavity radius was approximately 46 m and still growing at 0.527 sec. Shock-induced cracking was predicted to extend at least 237 m above the shot point. It was further pointed out that if the tensile strength of the rock materials would not permit a roof span of one cavity diameter to be stable, then the roof would collapse beyond the induced cracking zone or until the bulked rock filled the void to a point of equilibrium.
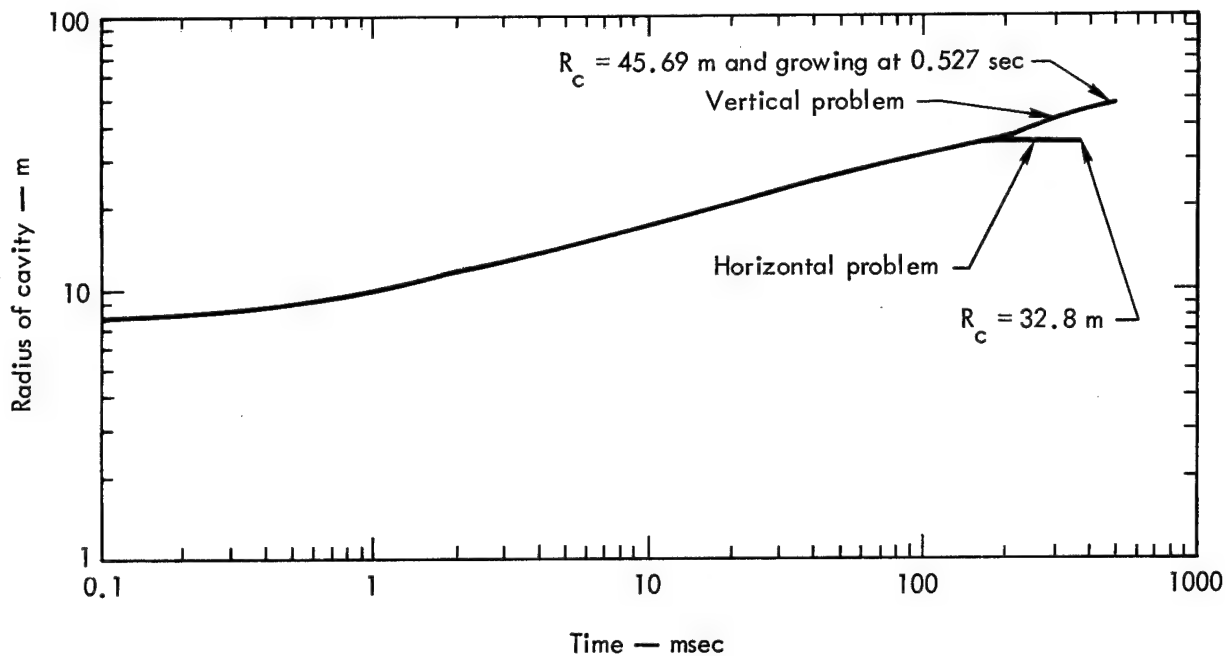
-15-

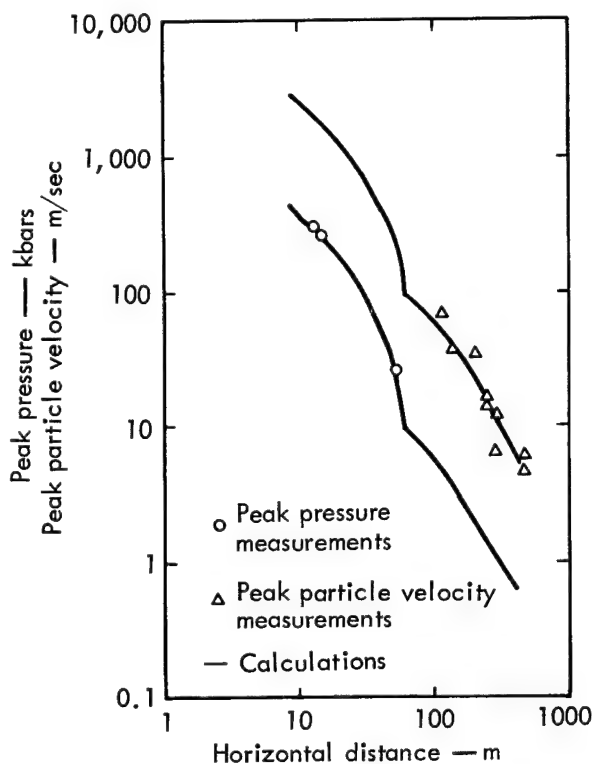Fig. 12. Calculated growth history of the Piledriver cavity.

Fig. 13. Peak pressure and peak parti-
cle velocity versus distance:
Piledriver Event.

Measurements (Ref. 9)

Chimney height was placed at 277 m
above the shot point, and the cavity radius
at 44.5 m. Calculated and measured peak
pressure and peak particle velocity are
compared in Fig. 13. The observed
measurements are consistent with the
vertical calculations, indicating that the
gas-acceleration role as currently simu-
lated has converged or is converging on
reality.

Salmon Event

Salmon was an approximately 5-kt
nuclear explosion buried at 827.8 m in the
Tatum Salt Dome near Hattiesburg,
Mississippi. It was detonated in October
1964. The salt dome consists of nearly
vertical beds of NaCl and $CaSO_4$ with a
composition of 90% NaCl, 10% $CaSO_4$.
The top of the dome is flat, about 375 m
below sea level and about 1600 m wide. It

Table II. Input data for Salmon preshot calculations (vertical component).

Parameter[a]	Salt	Anhydrite	Limestone	Sediments	
Overburden pressure at shot depth, kbar	0.181				
K, kbars	245	555	468	108	182
G, kbars	122	308	324	12.8	68
ρ_0, g/cc	2.2	2.92	2.5	2.0	1.9
T_0, kbar	0.01	0.01	0.01	0	0
K_0, kbar	0.600	0.20	0.1	0	0
K_1, kbar	0.100	0.10	0.1	0	0
K_2, kbar	0.050	0.05	0.05	0	0
Y_0, kbars	25	100	100	10	0
Y_1, kbar	0.500	0.1	0.1	0.005	0
Γ	1.5	2	2	2	2
Yield, kt	5.0				

			Salt Hugoniot			
p	μ	p	μ	p	μ
0	0.0	25	0.0828	300	0.53
1	0.00447	40	0.123	400	0.63
2	0.0085	60	0.173	600	0.795
5	0.02027	80	0.219	900	0.98
8	0.0318	100	0.255	1200	1.13
11	0.0426	150	0.34	2000	1.35
15	0.0554	200	0.41		

[a] K = bulk modulus; G = shear modulus; ρ_0 = initial density; T_0 = initial tensile strength; K_0 = dynamic elastic limit; K_1 = low-strain-rate elastic limit; K_2 = static elastic limit; Y_0 = confined crushing strength; Y_1 = compressive strength of cracked material; Γ = Grüneisen parameter.

is capped by approximately 140 m of anhydrite, above which is a few meters of gypsum, which in turn is overlain by about 38 m of limestone. Above these sediments is about 275 m of sand and clay (Ref. 10).

Calculations

One-dimensional SOC calculations were run vertically above the working point. The material parameters used in the calculations are summarized in Table II.

These first series of calculations (preshot) were performed by Rogers (Ref. 11); the following description is taken freely from his work.

Bulk and shear moduli were used which agreed with the experimental seismic compressional and shear wave velocities. The p-μ* data were based on static and dynamic

*Tables in which pressure is tabulated as a function of shock compression ($\mu = \rho/\rho_0 - 1$) for a material in its initial state and in its crushed state.

-17-

compressibility data for salt. The density used, 2.2 g/cm^3, was in agreement with laboratory analysis. A tensile strength of 10 bars was arbitrarily selected to indicate that the salt has some coherence on a large scale. The overburden of 181 bars at shot depth was added to this for determining the stress limit above which cracking occurs, so any reasonable value for the tensile strength has only a small effect on the calculated radius of cracking. The Tatum salt is impure, which implies a low bulk tensile strength. Anhydrite exhibits a sluggish phase transition in the pressure range of about 20 to 30 kilobars (kbars), and the effect of this on the 9% impurity in the salt was included in the code by setting the bulk compressive strength (Y_0) of the salt at 25 kbars. The input parameters for the overlying layers of anhydrite, limestone, and sediments were selected on the basis of data available at the time. No extensive p-μ curves were necessary for rock other than salt, since the pressure outside the salt dome was low enough to be described by the elastic constants and one point on the p-μ curve set to agree with the bulk modulus.

A postshot calculation was also made, with a new set of gas tables, to describe the central cavity pressure and with new experimentally determined compression data for the Tatum salt in the low-pressure range (40 kbars).

The value of the total internal energy in the material that will cause vaporization, E_v, used to determine the amount of salt vaporized is based on the waste heat concept, with the Hugoniot as the release adiabat and the heat of vaporization being about 1 kcal/g. For the 5 kt of energy dumped into a central sphere of iron gas of density 2.58 g/cc and 25-cm radius, the surrounding salt was vaporized to a radius of 3.7 m.

Subsequent calculations were started with the 5 kt of energy dumped into a central region of salt gas having a density of 2.0 g/cc and a radius of 2 or 3 m. With these inputs in the vertical calculations, the cavity growth stops at a radius of about 24 m in about 100 msec (Fig. 14). In the horizontal calculations, the cavity radius also goes to about 24 m in 100 msec, but then shrinks back to about 22 m at later time (250 msec). The pressure inside the complete cavity obtained from the preshot calculation was about 100 bars and less than the 181-bar overburden. The postshot calculation with the more accurate gas tables gave a value slightly higher than the preshot calculation, but the difference was not significant. Since the code does not include condensation or heat transfer, the real conditions at late time after the shot have not been completely treated.

As shown in Fig. 14, the salt was predicted to fail with the shock front up to about 25 m radius. The salt originally at 25 m is displaced to 35 m as the cavity expands. The failure associated with the shock front is directly related to the 25-kbar value used for the confined crushing strength (Y_0). A calculation was made with the value of Y_0 set high so that no failure could occur with the shock front. This calculation showed the material to exceed its tensile strength to about 33 m radius before any effects of reflected waves from overlying layers occurred. Whether the material fails by crushing or cracking depends on the interaction of crushing strength and tensile strength,
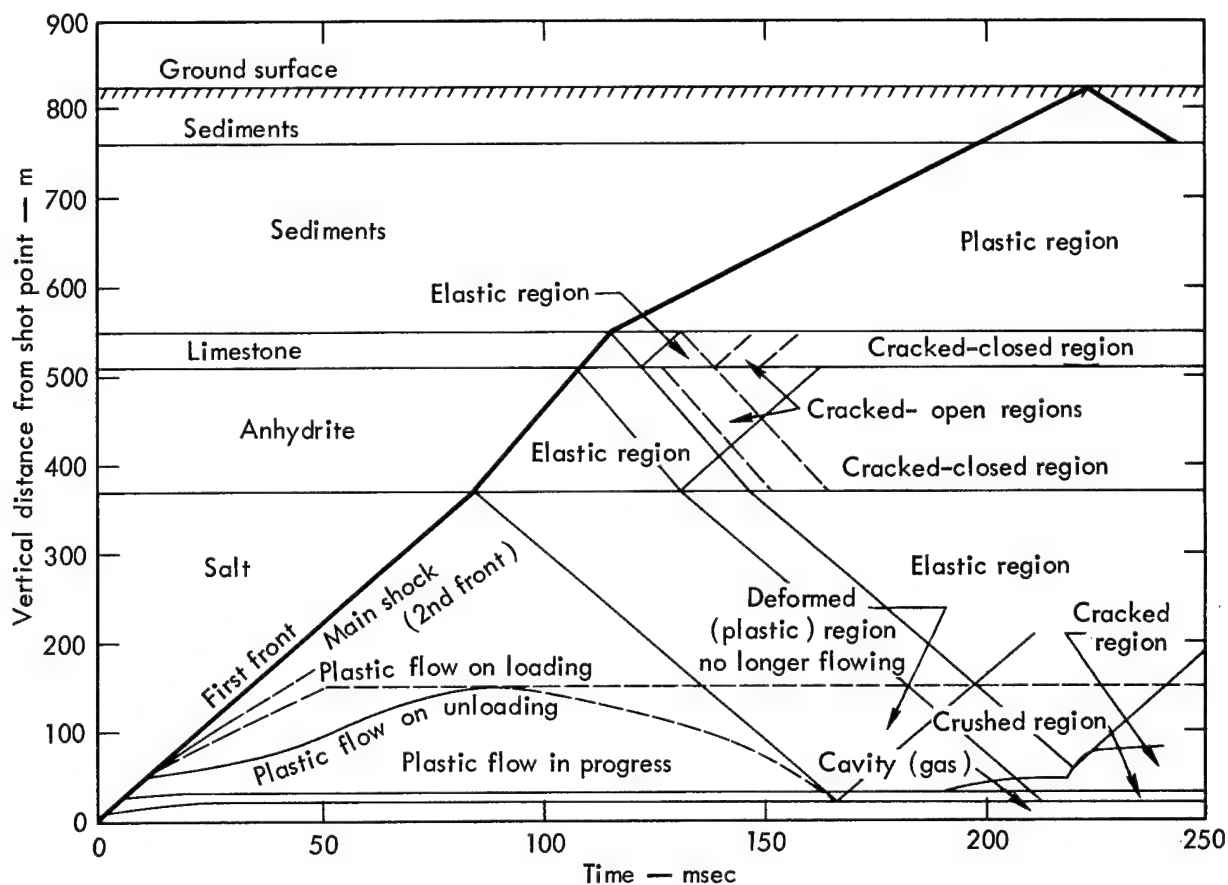
-18-

Fig. 14. Preshot calculations of shock-wave arrival times and rock alterations for the Salmon Event.

and in either case the material exhibits considerable plastic flow (Ref. 12). Cracks do not stay open very long, and in the real world (distinguished from the computer mathematics) any cracks found will close again by flow of the salt under overburden pressures. After the dynamic aspects of the explosion, the cavity will settle into static equilibrium, with the radial stress on the cavity wall dropping essentially to zero and tangential stress going into compression to sustain the overburden. If this tangential compressive stress is less than the strength of the material at the cavity wall, the cavity will remain open.

The plastic flow region (without actually cracking open) is controlled in the code primarily by the value of the low-strain-rate elastic limit (K_1), i.e., the maximum stress difference allowed for a material between principal directions for the cracked state of the material. The value of 100 bars was selected on the basis that the experimental tensile breaking strengths, where plastic flow would presumably start, were above this value. This stress limit is used on the rising part of the front when the code says it is no longer a sharply rising front and on the unloading region behind the shock front. The calculated time-distance history of

-19-

when the flow is occurring is also shown in Fig. 14 . On the basis of the 100-bar value for K_1, flow occurs out to about 150 m. The value of K_1 that best represents the Tatum salt is not known, however, and this value of 150 m might be on either side of the true value.

Calculated wave shapes for the intermediate range from the horizontal calculation are given in Fig. 15. Plots for a vertical calculation are similar, except that overburden is different for each radius, and waves reflected from the various boundaries complicate the late-time shape of the wave. The effect of the stress deviator K_S (the maximum stress

difference allowed between principal directions for dynamic conditions) in determining the magnitude of the precursor is seen in the "knees" in the plots.

The ground-surface vertical-motion calculations for a point directly over the shot point are shown in Fig. 16. These calculations involve the properties of all the material overlying the shot point, and agreement was fair only when more refined input data—"postshot"—were used.

Measurements

Calculations and experimental data for the arrival time of the shock front, or first disturbance, are compared in Fig. 17. The preshot and postshot calculations agree with experimental data, since all points fall on the same curve.

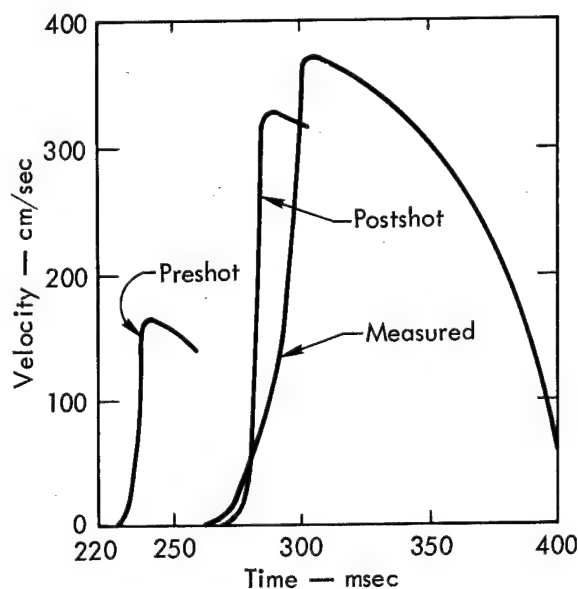Calculated peak velocity, peak radial stress, and displacement are compared

Fig. 15. Calculated radial-stress-wave profiles at several locations in the horizontal direction from the Salmon shot point .

Fig. 16. Calculated and measured vertical motion of the ground surface directly over the Salmon shot point.
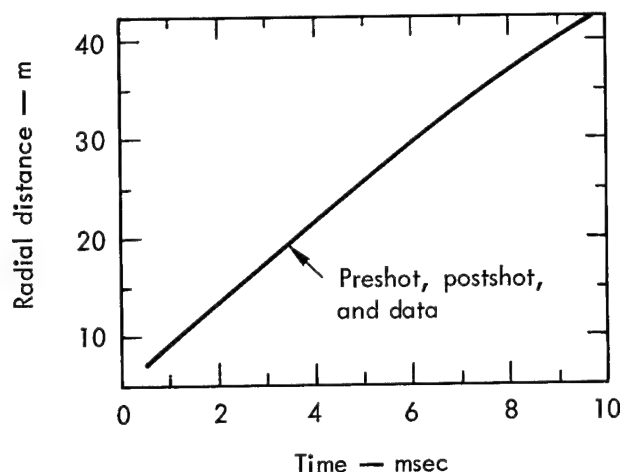
-20-

Fig. 17. Calculated and measured shock-wave arrival times near the Salmon shot point.
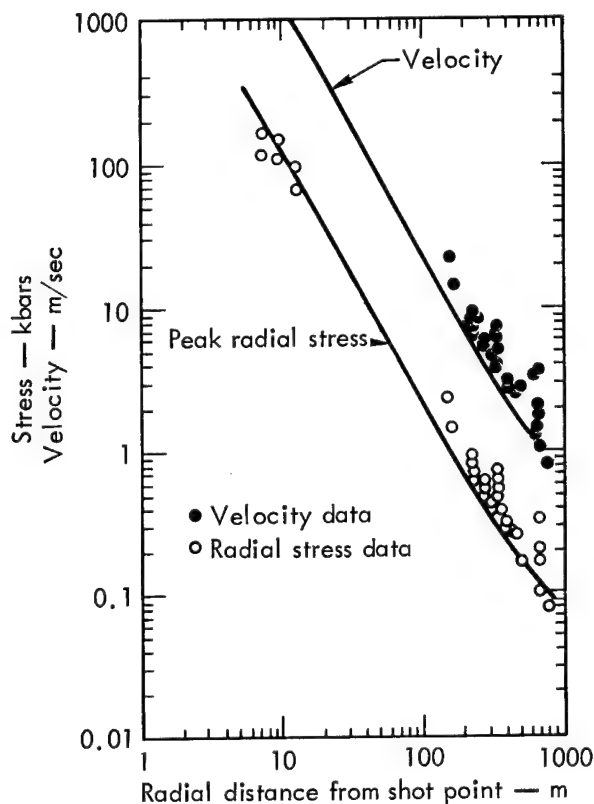

Fig. 18. Calculated peak radial stress and peak material velocity compared with field data from the Salmon Event.

with the field data in Fig. 18. The experimental data do not measure radial stress directly, but it can be approximated from the velocity data and the assumption that the wave is elastic with the stress given by

$$\sigma_r = \rho_0 C_0 U_p,$$

where

σ_r = radial stress,
ρ_0 = density,
C_0 = sound speed, and
U_p = particle velocity.

The calculations of peak velocity and peak radial stress are generally about 50% lower than the experimental data. The experimental ground-free-surface vertical motion shown in Fig. 16 is nearly matched by postshot calculations.

The cavity radius determined by pumping the cavity full of air was measured to be about 17 m. Measurements of the increase in pressure as a function of time and rate of air injection show that there is some additional volume, presumably in cracks or fissures connected to the cavity. The total volume of the fissures connected to the cavity is small compared to the main cavity volume (10 to 25%), and when this volume is added to the spherized cavity the radius is increased a few meters. The difference between 17 m and 24 m predicted by Rogers is not small. This anomaly was not resolved until refinements were recently made in the SOC input (Ref. 6).

The static elastic limit assumed by Rogers was 50 kbars. The failure model developed by Cherry et al. (Ref. 6), using EOS of Tatum salt material, allowed for a

-21-

brittle-ductile transition at 68 bars mean pressure. This implies a stronger salt and predicts a cavity radius of approximately 16 m, which agrees closely with the measured radius.

It is instructive to note that with a more accurate EOS and more sophisticated modeling, such as the failure models recently developed, the simulated phenomenology converges on the real world. This point was also confirmed when Cherry computed peak velocity and peak radial stress with the more accurate EOS of salt. Here there was better agreement with the measured data in Fig. 16.

Gasbuggy Event

The Gasbuggy experiment was conducted within a sequence of horizontal sediments at a depth of 4240 ft. The energy source was a 26-kt nuclear device. A generalized stratigraphy from the shot point to 3300 ft is:

Depth (ft)	Formation
3300 - 3650	Sandstone (Ojo Alamo)
3650 - 3800	Shale (Kirtland)
3800 - 3882	Shale-coal (Fruitland)
3915 - 4202	Sandstone (Pictured Cliffs)
4202 - shot point	Shale (Lewis)

This layered geometry dictated a need for careful equation-of-state descriptions of the Lewis shale and the Pictured Cliffs sandstone (Ref. 13). The shock Hugoniot data to approximately 680 kbars for Lewis shale and approximately 200 kbars for the Pictured Cliffs sandstone are illustrated in Fig. 19. The sediments above the Pictured Cliffs were tested to less than a few kilobars, since higher pressures were not expected at these levels. A description of the hydrostatic compressibility of the Lewis shale, Pictured Cliffs sandstone, and Fruitland coal in comparison with granite (Piledriver, Hardhat) and dolomite (Handcar) may be seen in Fig. 20. The criteria for material failure are derived and defined in Ref. 6, and are illustrated in Fig. 21. For a given material and a given mean stress, failure is defined when Y, a function of the material stress invariants, equals or exceeds the upper value of the material failure curve illustrated in Fig. 21. For example, failure will occur at a mean stress of 8 kbars in Lewis shale when $Y \geq 1.7$ kbars, and in the Pictured Cliffs sandstone when $Y \geq 3$ kbars. These data, along with the data in Table III, are the estimates of the parameters used to
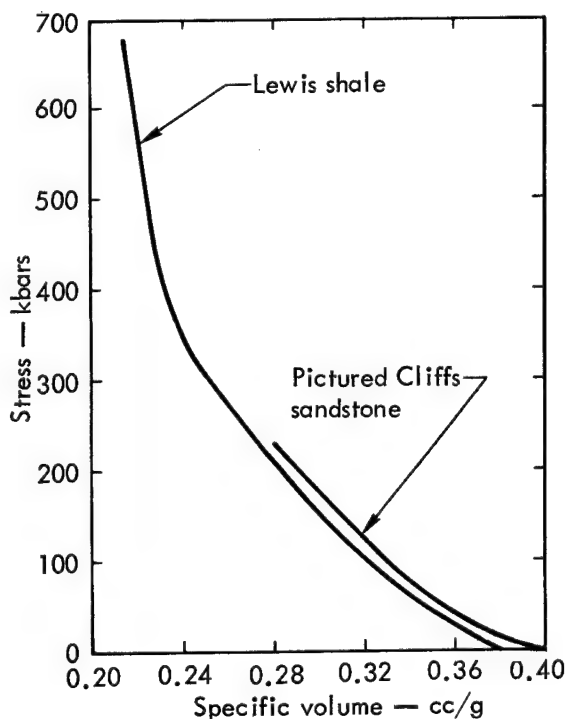

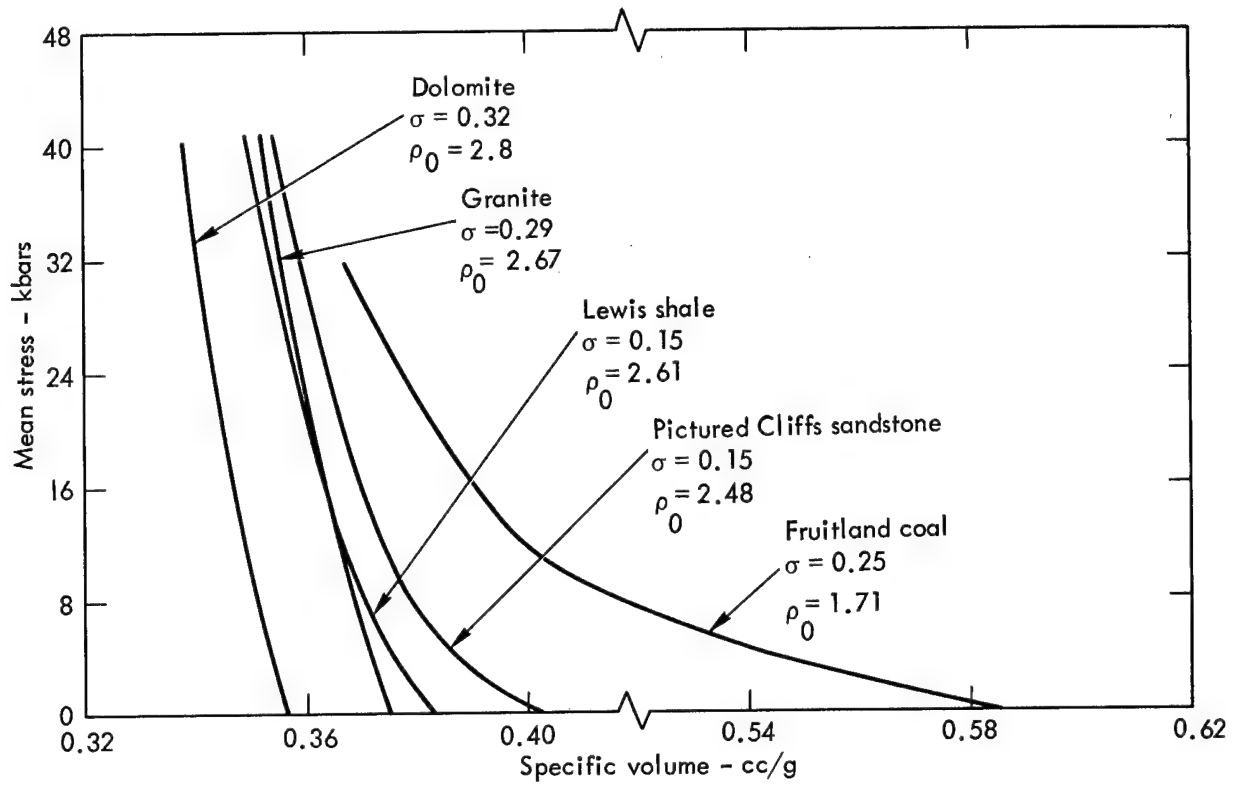Fig. 19. Hugoniot data for Lewis shale and Pictured Cliffs sandstone.

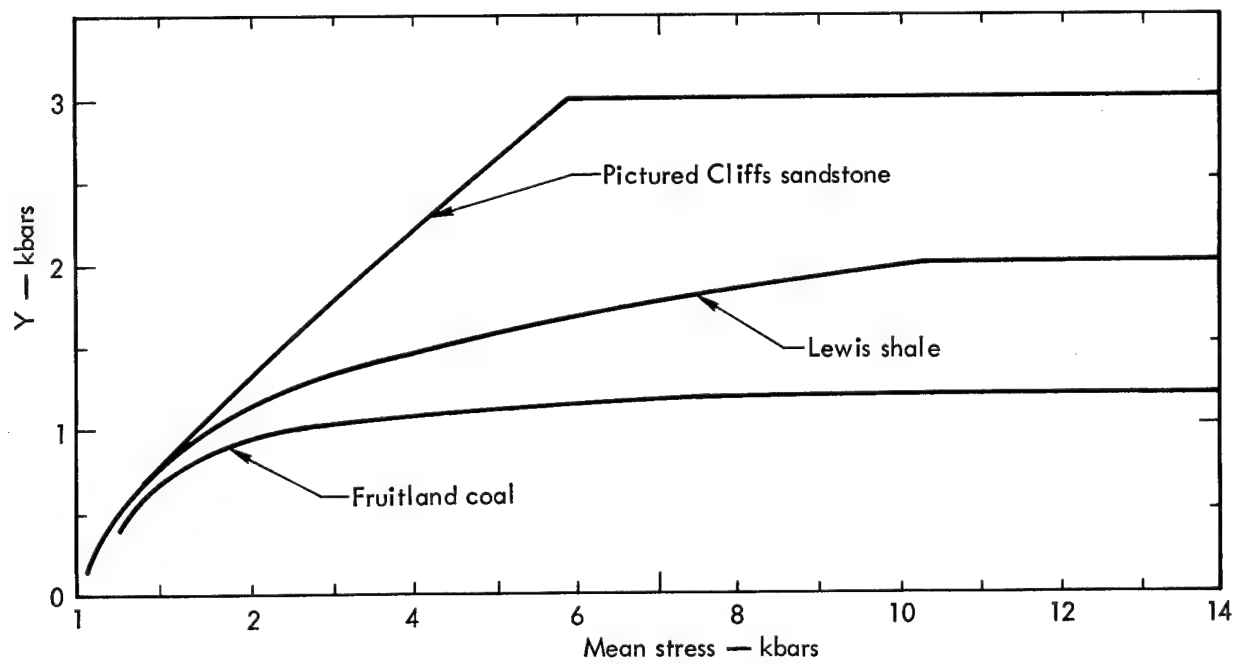Fig. 20. Hydrostatic compressibility of dolomite, granite, sandstone, shale, and coal.

Fig. 21. Material failure criteria for sandstone, shale, and coal.

generate the equations of state necessary for the Gasbuggy calculations.

Calculations

Two one-dimensional calculations using the SOC code were run (Ref. 3). The first treated all material above 3195 ft as Pictured Cliffs sandstone. This calculation predicted failure, i.e., cracking, out to approximately 390 ft, and a cavity radius of 78 ft.

The second run included the different layers above the Pictured Cliffs formation. Here material property differences, specifically those of the Fruitland coal, play a major role in determining the interaction of materials and source. Note the differences in density, compressional velocity, compressibility, and Poisson's ratio indicated in Table III. With these parameters now in the code, it was predicted that the highly compressible coal would act as an energy sink and in this way significantly lower the failure criteria below the values determined in the first calculations, at distances somewhere above the base of the coal. Based on these new input parameters, the chimney was predicted to extend only 334 ft vertically, stopped by the coal bed, but fractures could extend around the device up to 425 ft. Preliminary time-of-arrival data are compared with calculated data in Fig. 22.

Measurements

Postshot investigations by Korver and Rawson (Ref. 14) indicate that the cavity top is probably at approximately 3850 ft, or 325 ft above the working point, indicating a significant role played by the compressible coal in halting the chimney growth. The radius of fractures is estimated at 480 ft.

In general, there is very good agreement between measurements and those calculations which include the different rock materials above the shot point.

Cabriolet Event

The Cabriolet Event was a 2.5-kt Plowshare nuclear cratering experiment

Table III. Parameters used in generating equations of state for the Gasbuggy calculations.

Material	Region thickness (ft)	Density (g/cc)	Compressional velocity log (ft/sec)	Total water content (wt %)	Compressibility (Mbar)	Poisson's ratio	Heat of vaporization[a] (ergs/cc $\times 10^{12}$)	Heat of fusion[a] (ergs/cc $\times 10^{12}$)
Lewis shale	Shot point to 4202	2.61	13,700	3.5	0.191	0.15	0.4759	0.1259
Pictured Cliffs sandstone	4202 to 3915	2.48	13,520	4.5	0.134	0.15		
Fruitland coal	3915 to 3882	1.71	8,850		0.0602	0.25		
Fruitland shale	3882 to 3800	2.49	11,700		0.132	0.15		
Kirtland shale	3800 to 3650	2.58	14,070		0.240	0.15		

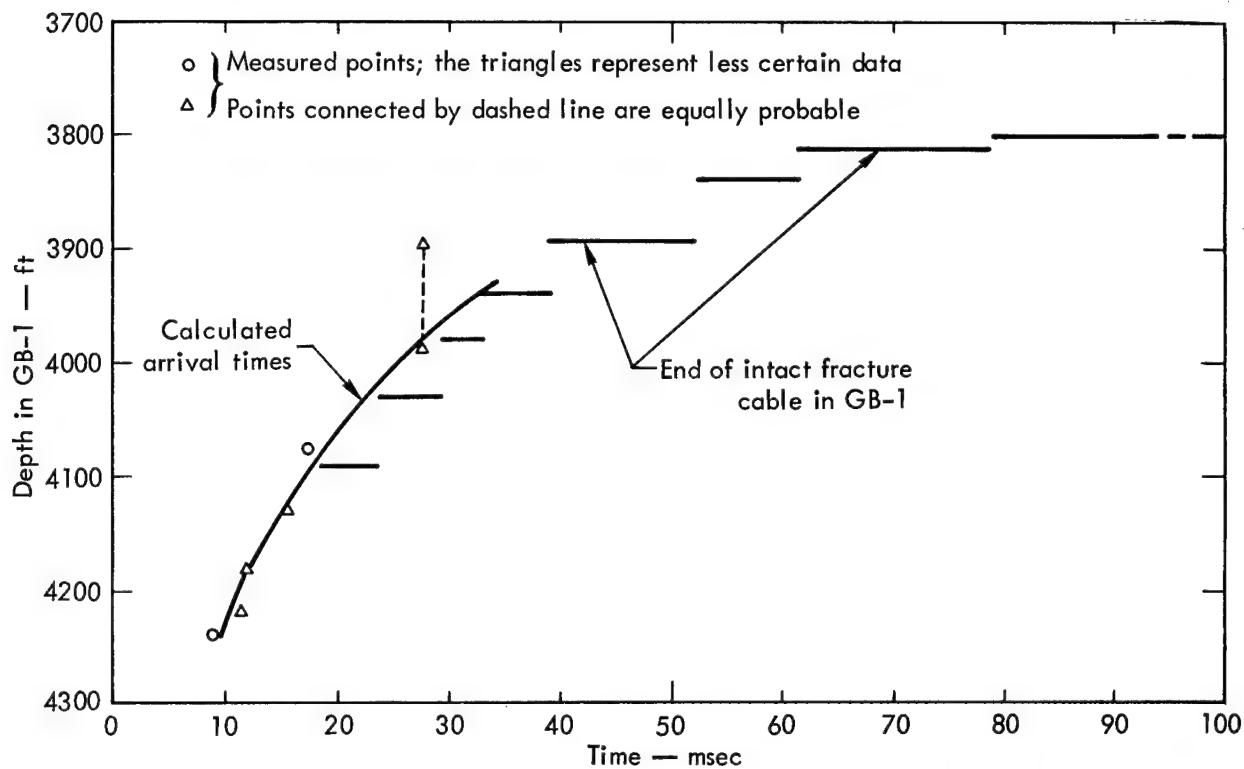[a]Heats of vaporization and fusion for SiO_2.

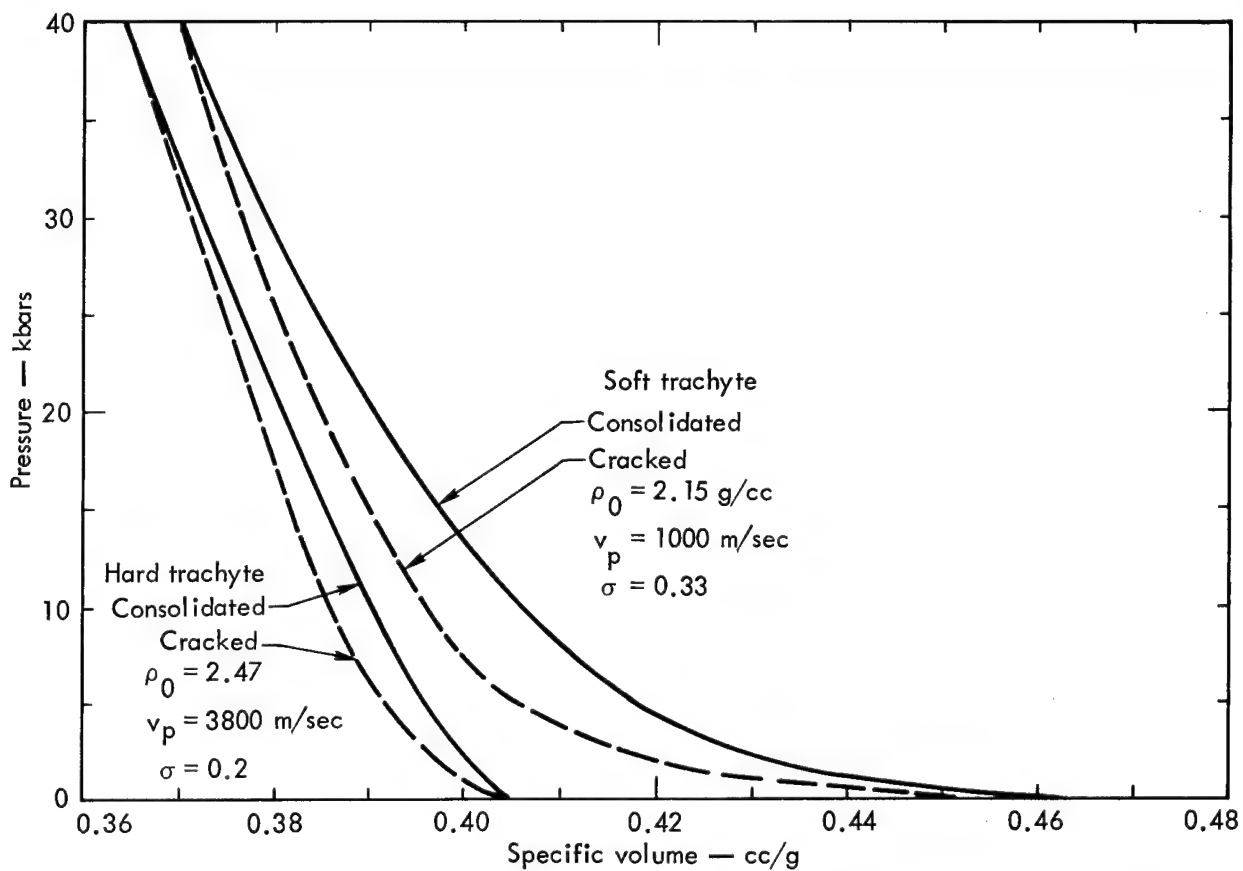Fig. 22.   Time of arrival of first motion at various radial distances.

Fig. 23.   Hydrostatic compressibility of consolidated and cracked soft trachyte.

in volcanic trachyte at NTS. It was detonated in January 1968.

Calculations

The basis for the Cabriolet calculations had already been established (Ref. 3).

Figures 23 through 25 summarize the in situ hydrostatic compressibility, seismic velocity measurements, and density measurements for the rocks at the Cabriolet site. The break in the velocity
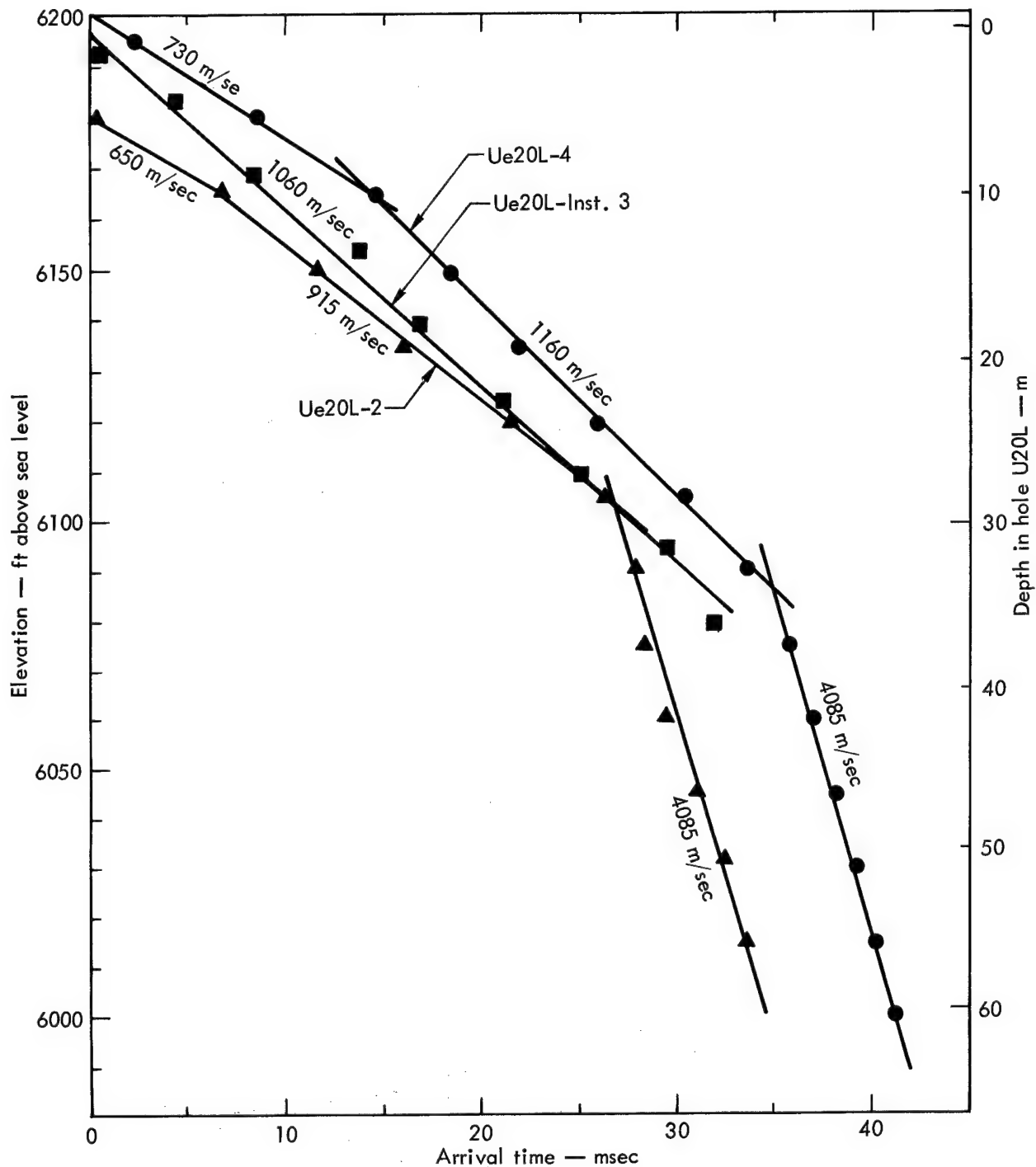
Fig. 24. Seismic velocity data from Cabriolet site.
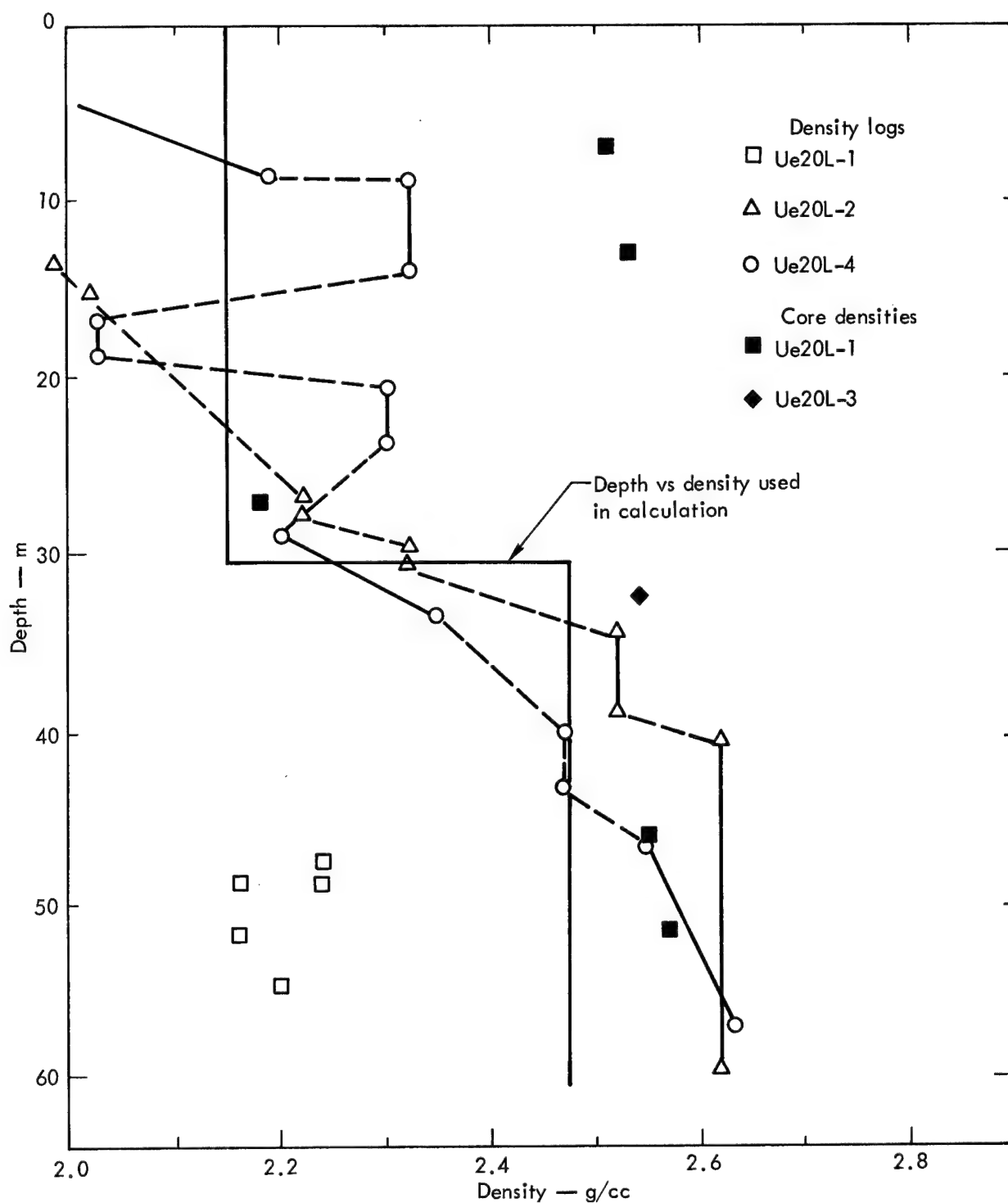
Fig. 25. Density measurements in the vicinity of the Cabriolet emplacement hole .

curves at 28 to 35 m from the surface was the criterion for selection of the density inputs indicated on Fig. 25.

Figure 26 is the predicted peak radial stress as a function of distance about the shot point. The particle velocity versus

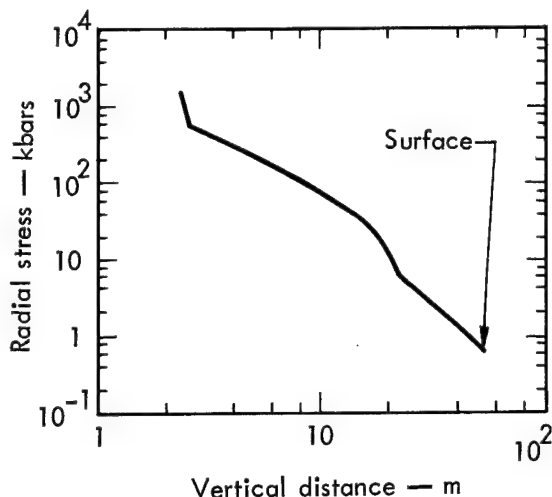distance at 135 msec is illustrated in
Fig. 27.

Fig. 26. Predicted peak radial stress as
a function of distance about the
Cabriolet shot point.

Figure 28 represents the throwout
calculation at 135 msec. All zones
whose velocities were great enough to
pass the free surface were removed
from the grid.

Cabriolet Code Verifications

Data collected on the cabriolet experi-
ment are still being reduced. The ap-
parent radius was 178 ft, compared with
a predicted 170 ± 40 ft. Preliminary data
from a slifer positioned 25 ft from the
emplacement hole indicate good agree-
ment between calculated shock position
and actual shock position as a function of
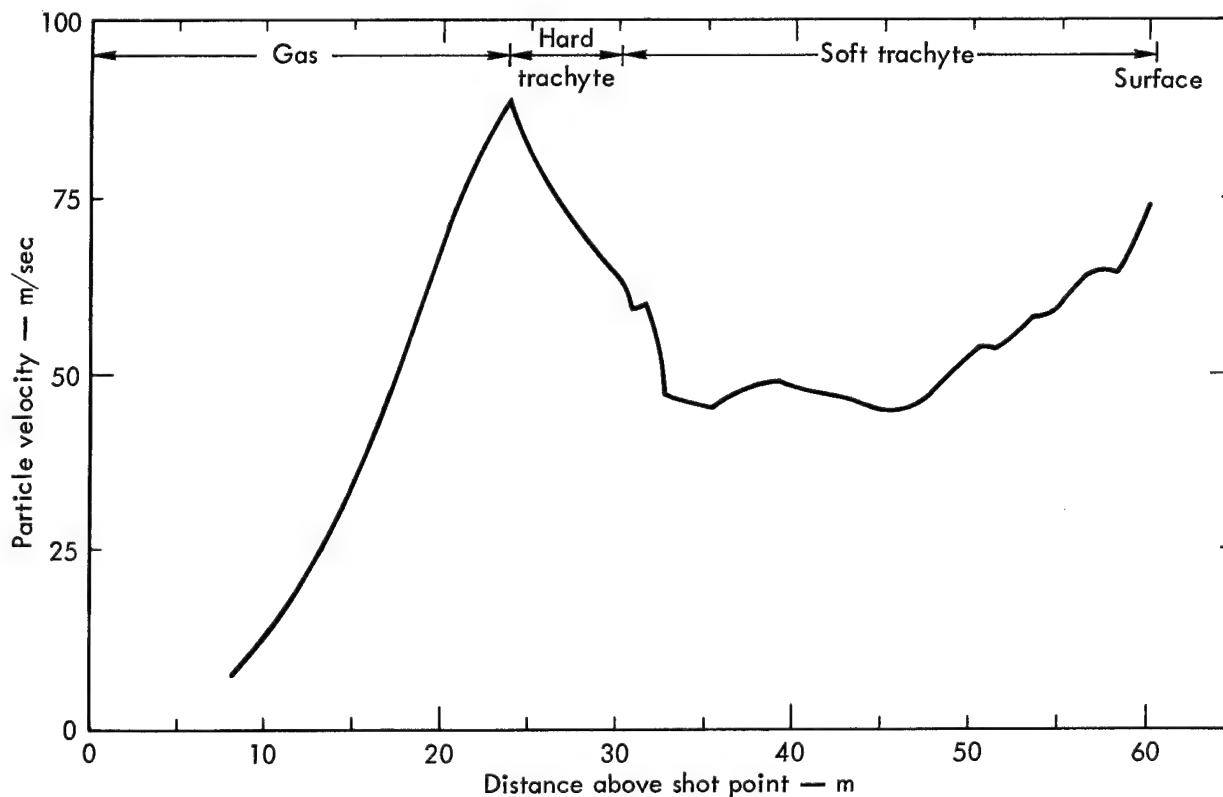distance and time.

Fig. 27. Calculated particle velocity versus distance above Cabriolet shot point at
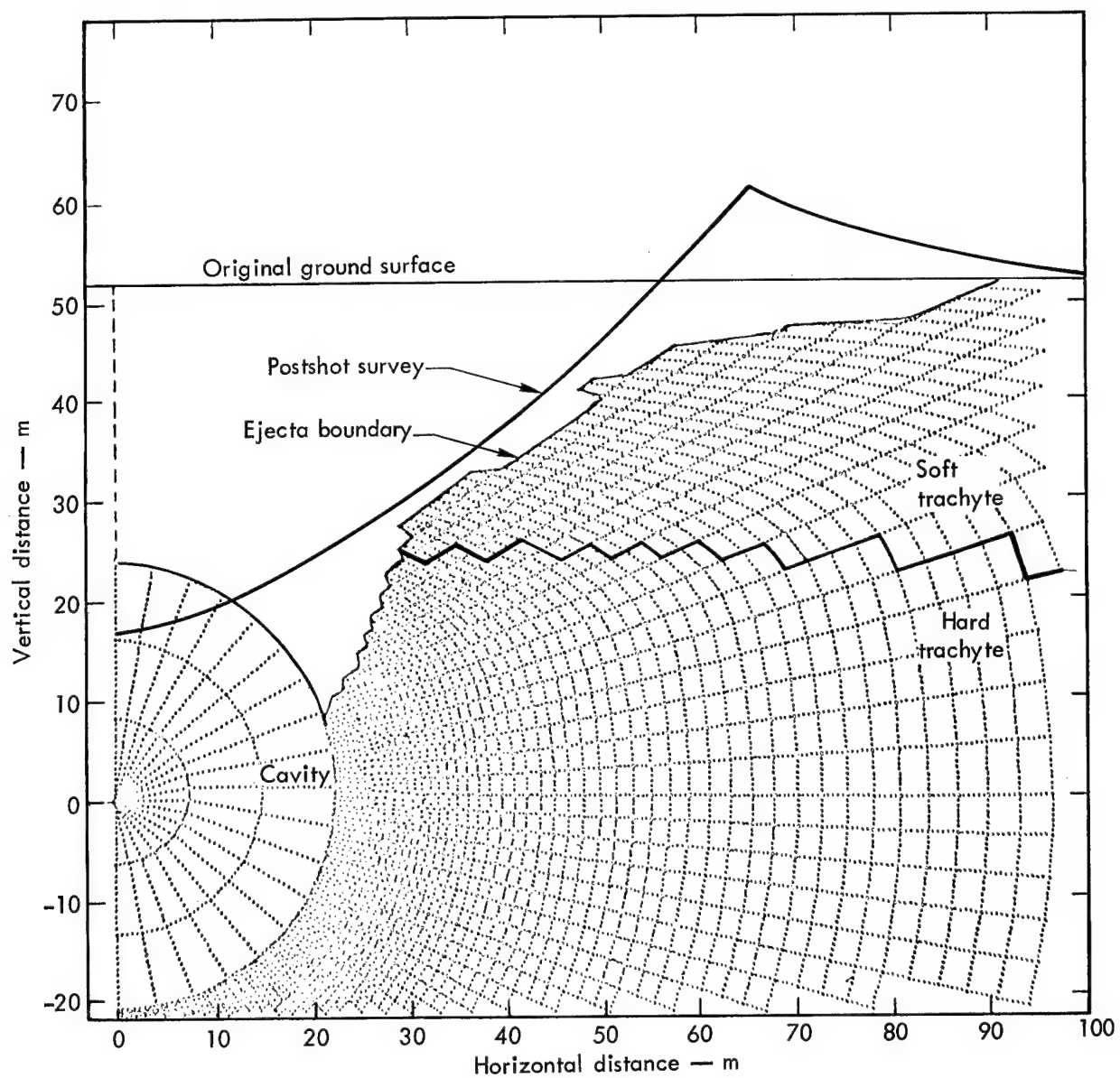135 msec.

Fig. 28. Throwout calculation at 135 msec for a 2.5-kt nuclear explosion in layered trachyte (cavity pressure = 48 bars).

Late-Time Phenomenology

CAVITY COOLING

Calculations

The cooling of cavities produced by nuclear explosions is being investigated by Chapin (Ref. 15) with two calculational models. The first model simulates the thermodynamics of the cavity from the time at which hydrodynamic expansion ceases (on the order of tenths of a second) until cracked material over the cavity drops into the cavity and collapse starts. The second model numerically describes the cooling of the cavity gas during collapse when relatively cool wall material is falling through the cavity.

Results of a SOC or TENSOR calculation are used to obtain the size and shape of the cavity and the energy and density of the cavity gas, which are initial conditions for Chapin's first cooling model. In this model, the following assumptions are made:

1. Gas properties are constant throughout the cavity, since rapid mixing is taking place.
2. The effect of natural convection in the cavity, which might induce thermal gradients in the gas, is small and can be ignored.
3. The material in the cavity is a binary mixture of SiO_2 and H_2O. (The best current equation of state is being used.)
4. The cavity gas is optically thick and emits blackbody radiation to the wall.
5. The wall is a perfect absorber. (Scattering properties of the gas and reflecting properties of the wall surface are not known.)
6. Convective and radiative heat transfer are independent.
7. The wall conditions are uniform.
8. Melted wall material is instantly removed from the walls, and all of the water contained in the melt is added to the cavity gas.
9. The cavity volume is constant.
10. All of the heat released from the cavity during condensation of the rock gas is due to the condensation process.

Starting with the initial conditions in the cavity as it is a few tenths of a second after the explosion (a pressure near overburden and a temperature of a few thousand degrees Kelvin), Chapin uses equations of state for SiO_2 and H_2O to determine the thermodynamic properties of the cavity gas. By calculating a heat transfer rate which includes radiation and convection, one determines the energy transferred to the cavity walls during a time interval Δt. The energy transferred to the walls is allowed to melt rock and vaporize water in the rock. The vaporized water is added to the cavity gas over the time Δt, and the increase of water density in the cavity is calculated. The increased density and decreased energy in the cavity at the time $t_0 + \Delta t$ result in a lowered temperature and pressure. This process is repeated by finite differences to obtain the time history of the cavity.

A point will be reached where the gaseous rock can condense. While the gas is condensing the heat-transfer rate is

held constant at its value just before condensation. All of the energy released by the cavity during rock condensation is assumed to be due to the condensation process, and the temperature of the cavity gas remains constant.

After the rock has condensed, the cavity is all steam; thus only the equation of state for water is needed. When the cavity temperature drops below the vaporization temperature of rock, heat transfer may be approximated by conduction into the walls. At this point, the TRUMP code (Ref. 16), which solves the heat-conduction equation with thermal-conductivity variables in space and time, can be used to calculate the heat-transfer rate. However, if a constant value for the thermal conductivity can be chosen, the heat-transfer equation and its boundary conditions in spherical coordinates can be simplified, and the heat-transfer rate can be calculated without TRUMP.

By using the heat-transfer rate due to conduction (from TRUMP or the analytical solution), Chapin's finite difference model can be continued to calculate the decrease in cavity pressure and temperature during the conduction phase.

Chapin's cavity-collapse model starts at a time when the cavity pressure is less than overburden. Collapse is visualized as a shower of debris into the cavity from the cracked material over the cavity. The model considers particles as they fall from the cavity roof. Each particle is allowed to trap some of the cavity gas in the bottom of the cavity, and the remaining gas in the cavity rises to replace the particle. The particles fall by gravity, and hence they remain in the cavity for a certain time. The particles are assumed to be spheres initially at a temperature T_0, and a rate for convective heat transfer to the particles from the cavity gas is calculated. This energy is then removed from the cavity gas. A rate and an average size at which particles enter the cavity are estimated. The rate of removal of mass and energy from the cavity gas can then be calculated. Using a water equation of state for the cavity gas, the pressure and temperature of the remaining cavity gas can be found. By advancing the equations with respect to time, the time history of the cavity gas as it rises to replace wall particles can be calculated. Comparisons between Chapin's model and experimental results are incomplete. Preliminary analyses indicate that good agreement can be achieved between the model and the observations discussed below (see Fig. 29).

Measurements

In one case where good cavity-pressure measurements were obtained from 45 sec postshot until collapse, simple Newtonian cooling of a steam-filled cavity was adequate to match the experimental data (Ref. 17):

$$(T - T_\infty)/(T_0 - T_\infty) = e^{-(hA/C_v n)t},$$

where:

t = time,

T = temperature at time t,

T_0 = T at t = 0,

T_∞ = T at t = ∞ (ambient temperature),

h = surface heat transfer coefficient,

A = surface area,

C_v = molar heat capacity at constant volume, and

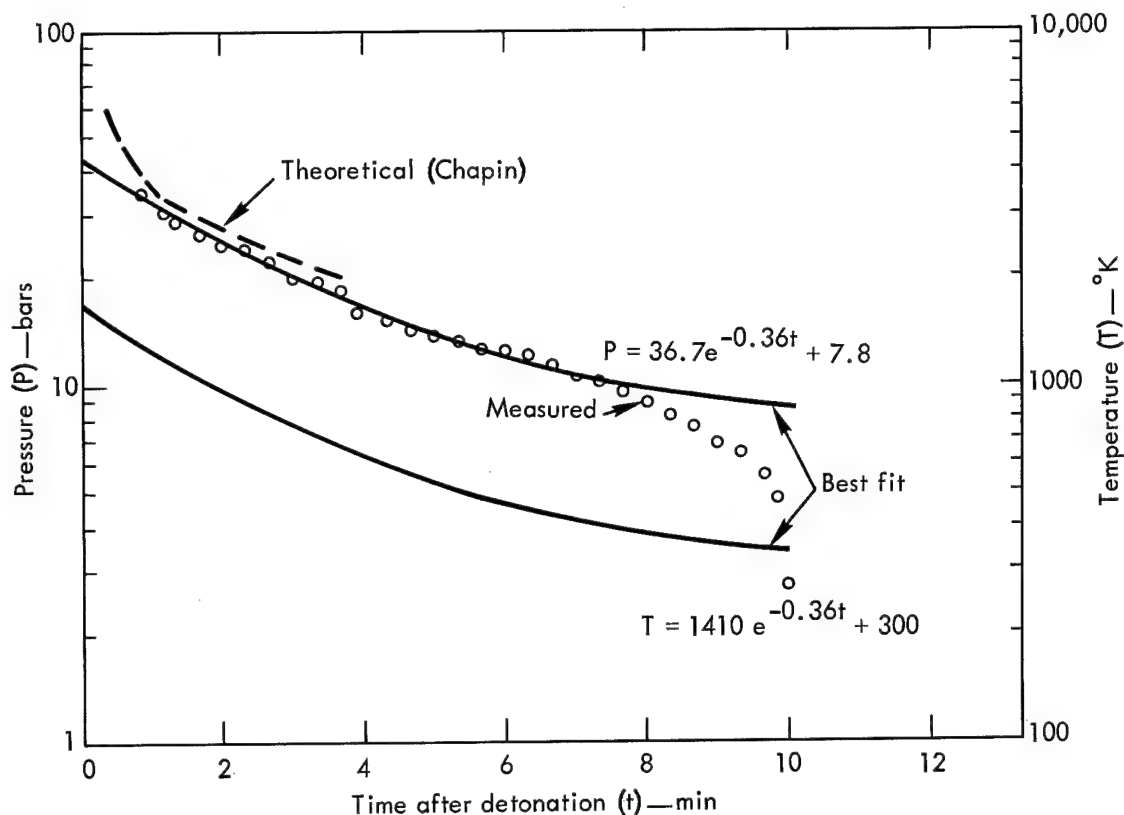n = total moles of material in cavity.

-31-

Fig. 29.   Comparison of measured pressure, theoretical pressure, and
best-fit pressure and temperature curves.

The Newtonian cooling calculation and the experimental values are compared in Fig. 29. Best agreement was obtained by assuming a heat-transfer coefficient of about 0.01 cal/cm^2-sec-°K. Note that at about 7 min after the shot, the measured pressure begins to deviate significantly from the best-fit curve. The deviation is probably the result of condensation of water vapor.

SEEPAGE OF RADIOACTIVITY

Calculations

The POROS code has been developed and successfully used by Rodean to simulate gas flow through porous materials (Ref. 18). POROS is one-dimensional with options for planar, cylindrical, or spherical coordinates; any set of units may be used. A number of boundary conditions may be applied to either the Darcy or the non-Darcy (laminar or turbulent) flow it calculates. The thermodynamic process may be adiabatic or isothermal throughout the system, or it may involve local temperature equilibrium between the gas and porous material. A POROS calculation could start at about the end of Chapin's cavity-collapse model, when heat transfer between the cavity gas and the rock particles is no longer significant.

Darcy flow assumes that inertial forces are negligible. The Darcy equation is a reduced Navier-Stokes equation which equates the pressure gradient with viscous

forces and potential body forces. In POROS, the body forces on the gas or fluid are also neglected, and only the viscous forces resist the gas motion. Darcy flow can be used for flows down to a Reynolds number of about 1, where the diameter of a grain size is used for the length parameter. The non-Darcy "turbulent" flow considered by POROS reduces to the Darcy equation by the use of another constant that effectively multiplies the permeability constant. POROS treats the viscosity of the gas, the Reynolds number, and the porosity and permeability of the sand as constants; however, it would require only a minor change to treat them as functions of thermodynamic variables or position.

POROS was used to simulate some laboratory tests of a high-pressure (250 psi) gas through 20 ft of typical sands used for stemming at NTS. Pressure-vs-time histories were both measured and calculated at stations located 5, 10, 15, and 20 ft from the initial gas/sand interface. Results compare very well for the 5- and 10-ft stations, but differ slightly at the 15-ft station and more at the 20-ft station. Generally, the "turbulent" non-Darcy calculations give better agreement with the data.

Measurements

Although the agreement between calculations and the laboratory experiments cited above is promising, there have been no meaningful comparisons between POROS calculations and data from nuclear shots. While we expect this calculational tool to be of increasing use in the future, at present one must seek an understanding of seepage of radioactivity by examining our field experience.

Delayed seepage of radioactivity may occur in an otherwise contained underground nuclear shot as a result of the upward travel of radioactive gases in the chimney which forms by progressive collapse of the material overlying the initially produced cavity. Aron (Ref. 19) has reviewed data from 28 underground nuclear shots of yields ranging from a fraction of a kiloton to approximately 1000 kt, to examine the relationship between nuclear explosive yield and the height to which radioactive gases rise in the chimney. The following is taken freely from Aron's work.

The 28 events were chosen according to the following criteria:

1. The postshot hole drilled to determine the height of radiation in the chimney must have been drilled vertically down into the chimney within one cavity radius of a vertical line through the working point (most postshot holes prior to mid-1964 met this requirement), or, if the postshot hole was drilled at a slant from the outside the chimney, the bit must have entered the chimney at a height above that at which radiation was detected.

2. A record must have been available of the depth of the bit at the time radiation was detected.

Relationship Between Yield and Rubble Volume

The radioactive gas propagates up the chimney toward the surface by displacing the collapsing chimney rubble and by diffusion. As a result of heat transfer between the hot gas and cold rubble, the gas

-33-

is cooled and finally condenses. There-
fore, the larger the yield, the greater the
amount of gas and the more rubble neces-
sary to condense the gas.

It was assumed for the purpose of this
study that the cavities were spherical,
that the chimneys were right circular
cylinders with the same radius as the
cavity, and that the gradation of the
chimney rubble was the same for all
events. Thus, the chimney volume, V,
up to a height, h, above the working point
can be computed as:

$$V = \frac{2}{3} \pi R_c^3 + \pi R_c^2 h,$$

where

R_c = the cavity radius.

There is usually a considerable uncertainty
in the cavity radius. It is clear from the
above formula that large uncertainties in
radii will produce large uncertainties in
chimney volumes. In addition, cavities
are not always spherical.

The data give one of two possible values
of h: (1) the location of the bit when radio-
activity is first detected at the surface;
or (2) the location of the bit when loss of
circulation of drilling fluid (LOC) occurs.
LOC always occurs either at the same
level or higher than the location of the bit
when radioactivity is first detected at the
surface. Since we wish to arrive at a
conservative relationship between yield
and the volume of rubble necessary to
quench the contaminated gas and stop
movement of noncondensable gases to the
surface, we shall assume that a column
of rubble at least up to the LOC point is
required. An envelope can then be

derived, such that it gives a volume
greater than that of the rubble column up
to LOC for all cases. This envelope can
be expressed as

$$V = 4.67 \times 10^6 \, W^{0.754}, \tag{4}$$

where

V = volume in ft^3, and

W = yield in kt.

For events with yields less than 10 kt,
the volume-yield line approximates the
surface of the earth. However, for
higher yields, the line is generally below
the surface. This means that by using
the present depth criteria, radiation will
not rise as close to the surface for higher
yields as for lower yields. If data with
less uncertainty were available for the
depth where radiation was encountered,
this conservative line could be moved
downward and thus be even more mean-
ingful.

Maximum Depth of Burial at which Radiation will Rise up the Chimney to the Surface

Another way to examine the volume of
chimney rubble is to plot, for various
yields, the maximum depth of burial at
which radiation will propagate up the
chimney to the surface. This depth is
computed as follows: The volume, V, of
rubble in the chimney up to the height, h,
to which radiation rises is

$$V = \frac{2}{3} \pi R_c^3 + \pi R_c^2 h = \pi R_c^2 \left(\frac{2}{3} R_c + h \right). \tag{5}$$

Using the predicted cavity radius for tuff,
R_{cp},

$$R_{cp} \approx 312 \frac{W^{1/3}}{(\rho d)^{1/4}} \qquad (6)$$

where

W = yield in kt,

ρ = density in g/cc, and

d = depth of burial in feet.

We substitute in Eq. (5) to get

$$V = \pi(312)^2 \frac{W^{2/3}}{(\rho d)^{1/2}} \left[\frac{2}{3} \left(312 \frac{W^{1/3}}{(\rho d)^{1/4}} \right) + h \right]. \qquad (7)$$

Now if we let d equal h and assume that ρ = 2.1 g/cc, we get, after some algebriac manipulation,

$$V = 2.13 \times 10^5 \left(\frac{168\, W}{h^{3/4}} + W^{2/3}\, h^{1/2} \right). \qquad (8)$$

By using Eq. (4), the curve for tuff in Fig. 30 can be drawn. The alluvium curve in Fig. 30 was drawn in similar manner, except that the predicted cavity radius and density were:

$$R_{cp} = 296 \frac{W^{1/3}}{(\rho h)^{1/4}},$$

$$\rho = 1.9 \text{ g/cc.}$$

The dashed parts of the curves represent extrapolation, since there is little or no experience with those yields in that soil material. These two curves represent the minimum depth of burial necessary to create sufficient chimney rubble to quench and to stop the displacement and diffusion of the contaminated gas up the chimney.
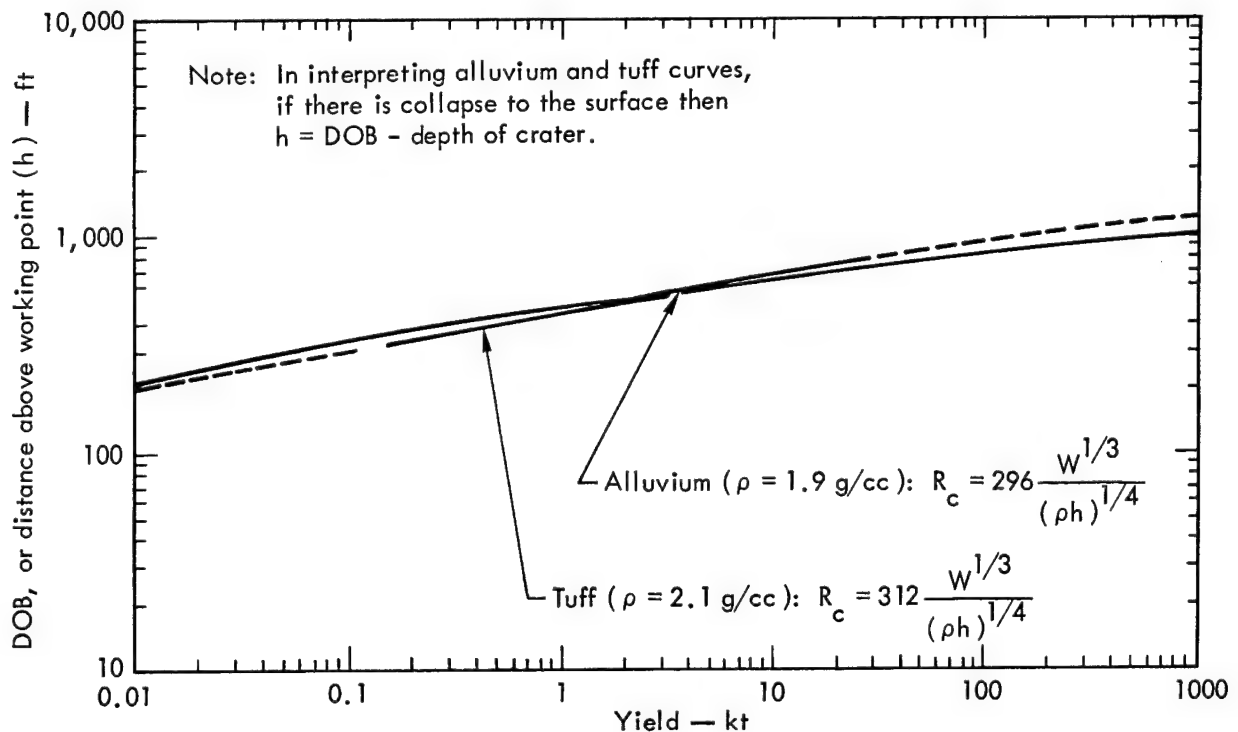
Fig. 30. Calculated maximum depth of burial (DOB) at which radiation will rise up the chimney to the surface in alluvium and tuff

Although it would appear that the curves derived in Fig. 30 are very conservative as a result of using Eq. (4), a few words of caution are in order. Cavity radius for individual events cannot be predicted very accurately. Also, there will be errors in estimating average overburden pressure because of lack of detailed knowledge of density. The distance from the working point to the postshot surface is not the depth of burial, d, as assumed in Eq. (4), but rather d less the depth of the crater formed. When Fig. 30 is compared with current practice, we can conclude that current practice is conservative below 1 kt and above 10 kt, and realistic in the region between 1 and 10 kt. However, this is exactly the

region where most of our experience lies, and, as we point out in the opening section of this paper, only a few events in this region have seeped a significant amount of radioactivity.

Distance from Surface to Top of Radioactivity in Chimney

Figure 31 illustrates another method of demonstrating with the available data that venting by the propagation of gas up the chimney is less probable at high yields. This figure is a plot of distance from the surface to where radiation was first encountered as a function of yield. Since there is considerable uncertainty in the radiation location, the curve is drawn to be conservative.
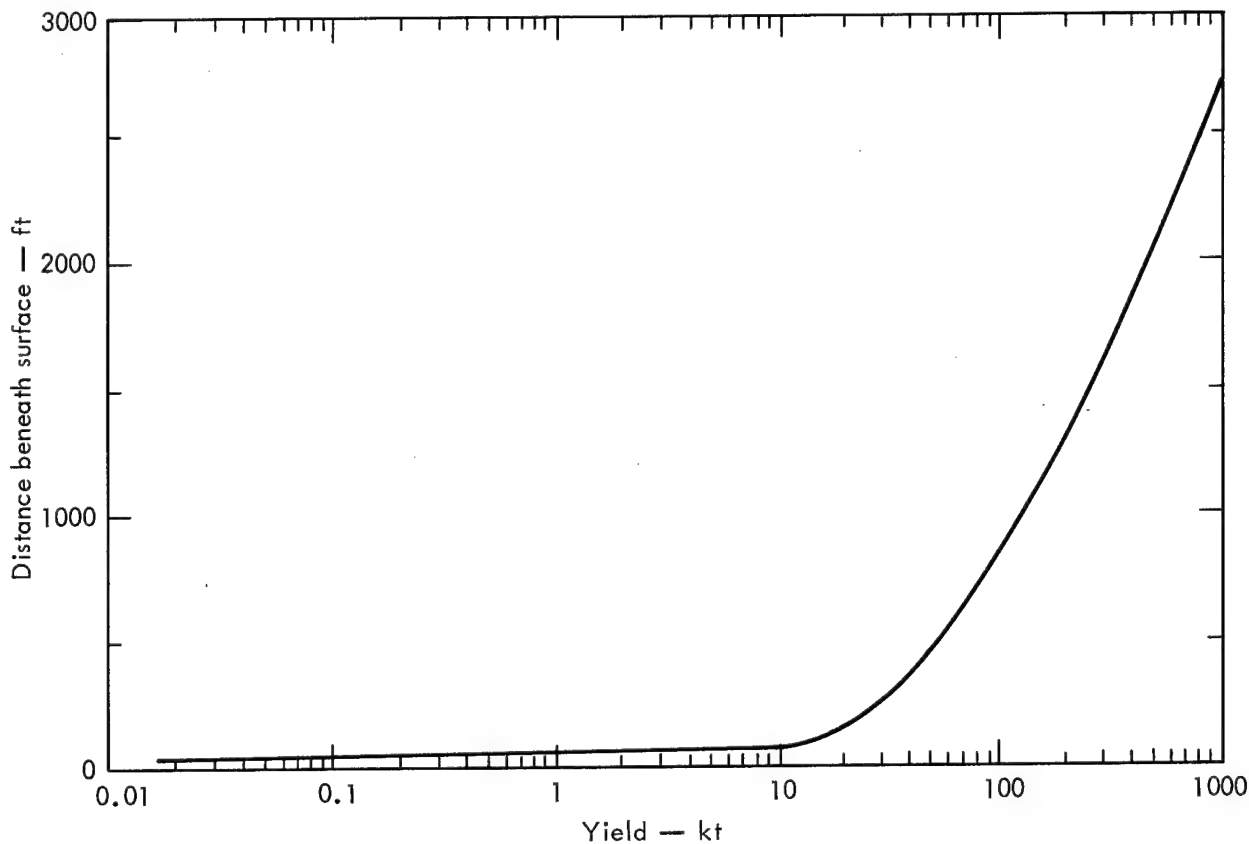

Fig. 31. Distance from surface to top of radioactivity in chimney.

The information in this figure is independent of cavity radius; therefore, the uncertainty in cavity radius does not hinder its interpretation. This figure shows again that for yields above 10 kt the distance between the surface and detectable radiation increases with yield.

Conclusions

There appears to be a relationship between yield and volume of rubble necessary to quench the condensable contaminated gases rising up the chimney to contain the noncondensable contaminated gases.

At yields greater than 10 kt, the distance between the surface and the highest point to which radiation rises up the chimney becomes greater as the yield increases.

Seepage due to radiation propagating up the chimney during collapse is less probable for yields greater than 10 kt, and the probability decreases as the yield increases.

Containment and Geological Structures

Structures which may be potential vent paths are the man-made discontinuities formed by the drilling of emplacement or instrument holes, or the geological discontinuities of faults or joints. The man-made discontinuity is resolved by carefully stemming the holes with sand and gravel, grout, or combinations of these. The properties of the stemming materials are matched as nearly as possible to the properties of the surrounding rock. There have been few problems in this specific engineering area. Emplacement holes can, and have been, successfully stemmed, and with few exceptions they have not acted as vent paths.

Whereas the positions of drilled holes are known within inches, the positions of faults are much less precisely known. Fault motion cannot be predicted with confidence. Our operational procedure has been to avoid emplacing explosives on or immediately adjacent to known major or sensitive faults. We follow this policy not because we can predict with certainty that these sites would generate vent paths, but simply because it eliminates any possibility that they might.

SURFACE FRACTURE PATTERNS AND THEIR ORIGINS

Geologic fracture patterns associated with underground nuclear explosions fall into three general types:

Radiosymmetric fracture patterns — This group includes both radial and concentric fractures that combine to form a pattern whose center of symmetry is ground zero. Individual fractures may be as long as a few tens of feet, and the whole pattern usually extends up to $500 \, W^{1/3}$ ft. The fractures are caused by doming, spalling, and collapse.

Bisymmetric fracture patterns — These are fractures with a strong preferred orientation, more or less bilaterally symmetrical with respect to a surface line through ground zero. They are usually

tens of feet long but may be several hundred feet long; the pattern may extend up to $1000 \, W^{1/3}$ ft. These fractures are thought to be controlled by joints.

Linear fracture patterns (Ref. 20)— Linear-fracture zones may range from a few feet to several hundred feet wide and from a few feet to thousands of feet long. These fractures are thought to be most likely associated with faults and therefore extend to depths of hundreds to perhaps thousands of feet.

The above generalized descriptions of fault or fracture patterns are of little help in predicting containment or dynamic venting. For the purposes of containment, it has been suggested that the terms "sensitive" and "insensitive" be applied to faults as a guideline for their motion potential. "Sensitive" is understood to apply to those faults along which an explosion causes or triggers some displacement for thousands of feet. "Insensitive" applies to all other faults.

Sensitive faults cannot be positively indentified without a large nearby explosion, nor can the mechanisms of motion be expressed rigorously. Hence, it is impossible to predict fault motion. It appears that sensitive faults are those which have had motion in recent geological time—i.e., the past million years.

YUCCA FLAT FAULTS

Yucca Flat is a 10-by-20-mile area covered with alluvium. Tertiary tuff underlies the alluvium, and the tuff is underlain by carbonates. The valley is surrounded by hills of tuff which are underlain by pre-Tertiary sediments and intrusives.

Two typical cross sections through the valley are shown in Fig. 32. The unconformable relation of the alluvium resting on the tuff, which in turn rests on the pre-Tertiary rocks, is clearly seen.

Motion Studies

1962 to 1965

During the period of 1962 to 1965, the U.S. Geological Survey studied the motion of faults in Yucca Flat as a result of nuclear tests by examining surface areas adjacent to ground zero before and after the tests. The two predominant sensitive faults in Yucca Flat are the Yucca Fault and the Area 3 Fault (Fig. 33). The Yucca Fault extends north and south probably the whole length of the valley. In its northern extension, the surface expression is a 20-ft escarpment in alluvium. The vertical displacement on the east is 100 ft in tuff. The downthrown side in both instances is on the east. The Area 3 Fault trends approximately north 10° east and is about 2 miles east of the Yucca Fault in the middle of the valley. There is little surface expression of this fault.

Dickey (Ref. 21) reports that faulting on the Yucca Fault and Area 3 Fault due to nuclear explosions is expressed as small vertical displacements, perhaps several inches, or as cracking extending for thousands of feet, with no vertical displacement. Table IV summarizes significant data on the effects of 16 shots fired in the vicinity of these faults. Among the 16 events instrumented, fault motion was observed in nine; of these nine, one vented. Visible ground heaving,
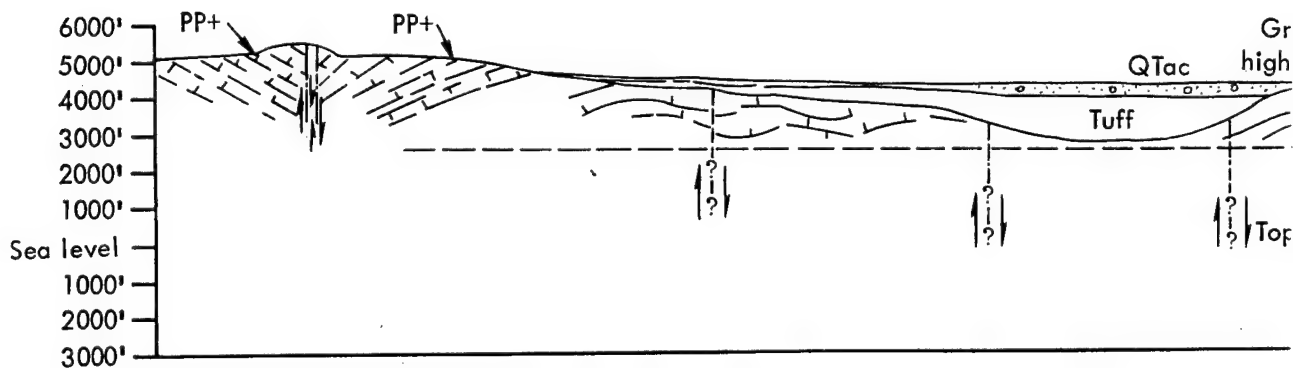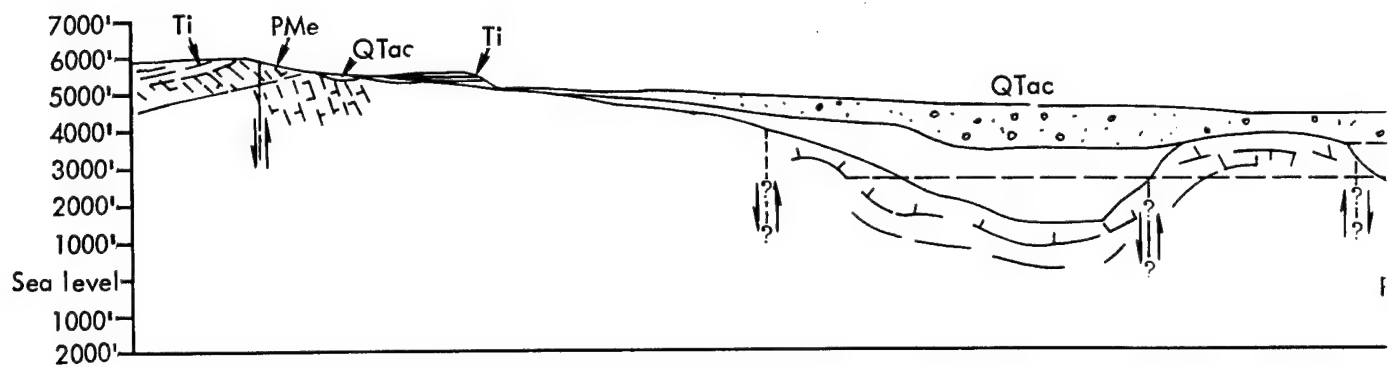
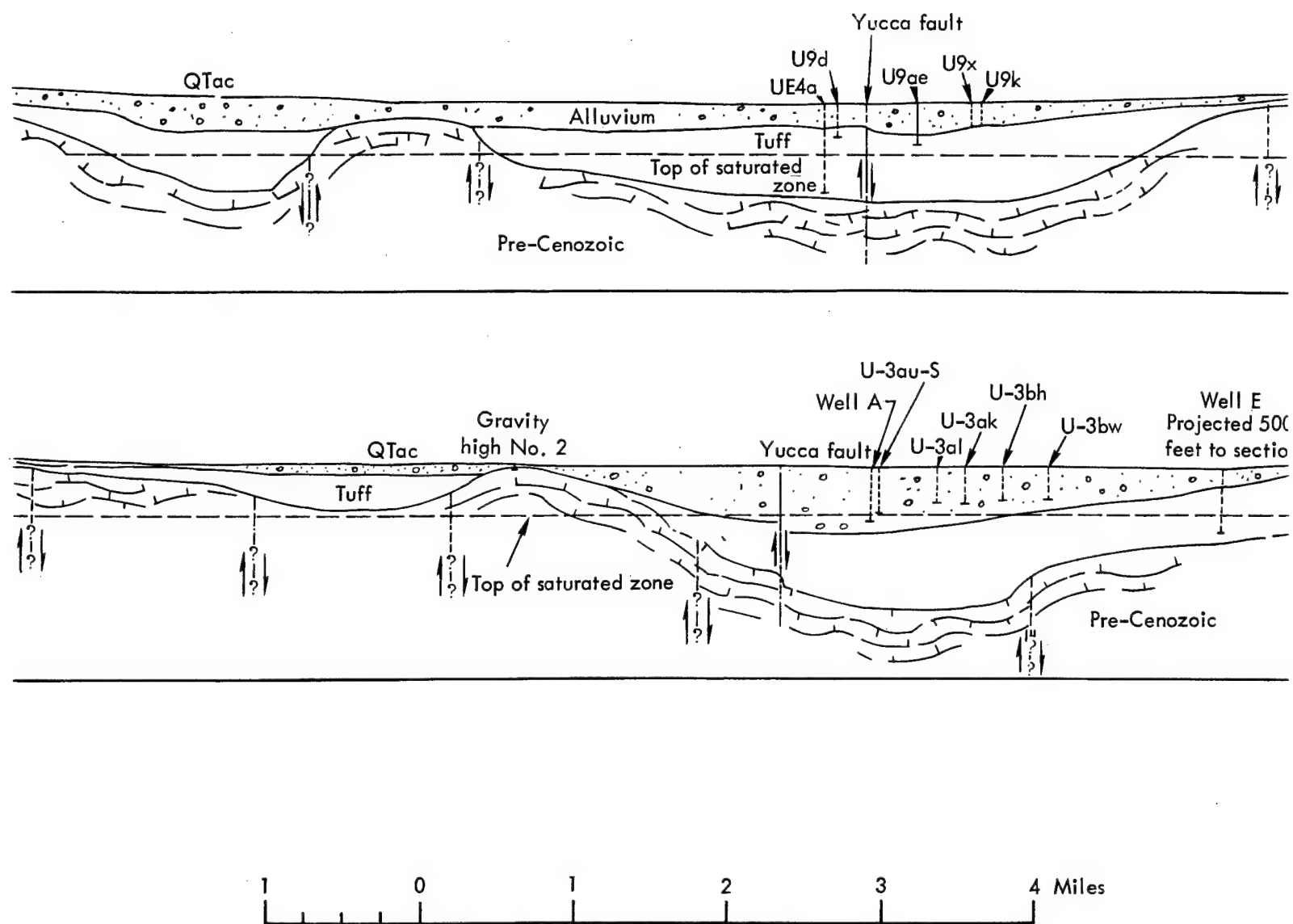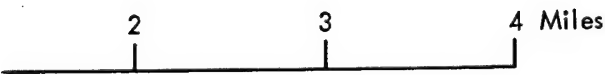Fig. 32. Typical cross sections th

Fig. 32. Typical cross sections through Yucca Flat (U. S. Geological Survey).

Yucca fault

U9d
UE4a
U9ae
U9x
U9k

QTac

Tpi QTac
Tp
Tp
Tp

ium

Tuff

Top of saturated
zone

7000'
6000'
5000'
4000'
3000'
2000'
1000'
Sea level
1000'
2000'

U-3au-S
Well A
U-3ak
U-3bh
U-3bw

Well E
Projected 5000
feet to section

Tp

Op

Yucca fault
U-3al

Op

zone

Pre-Cenozoic

6000'
5000'
4000'
3000'
2000'
1000'
Sea level
1000'
2000'
3000'

2   3   4 Miles

cca Flat (U. S. Geological Survey).

③
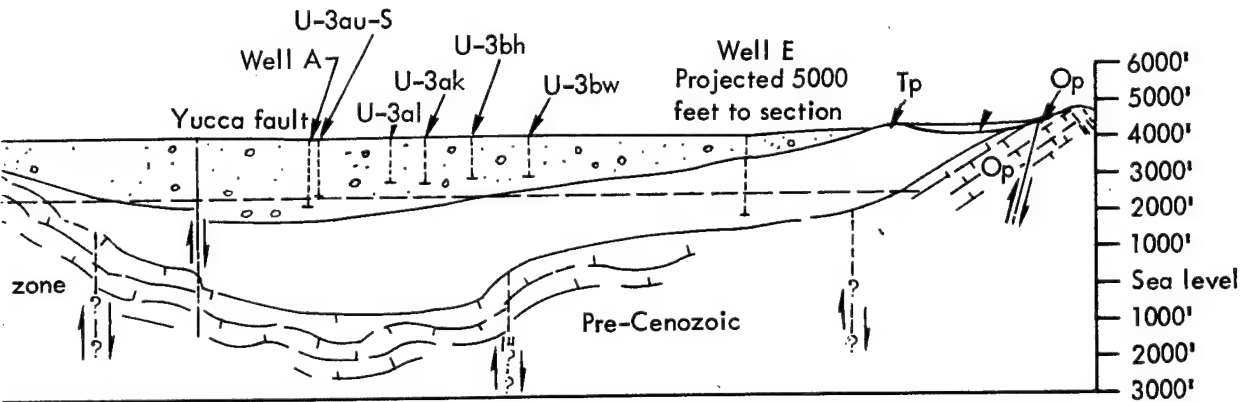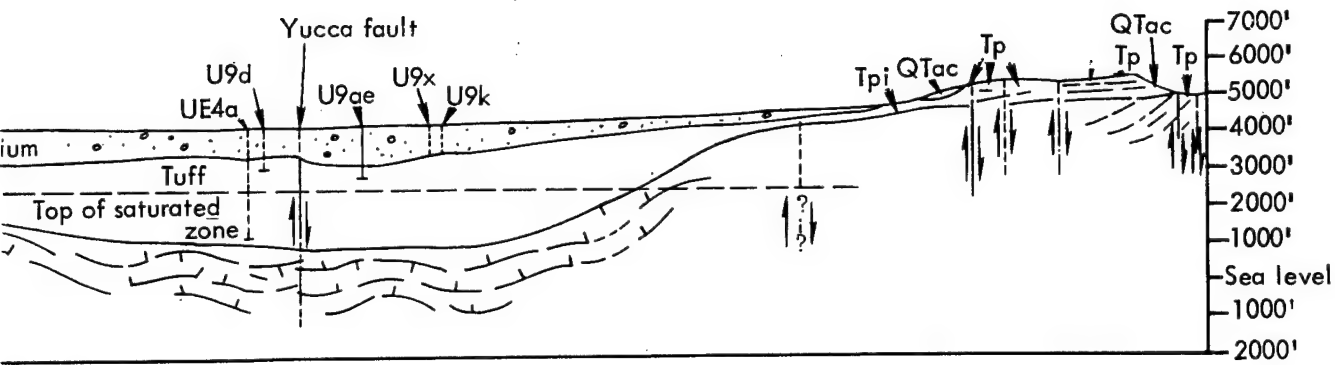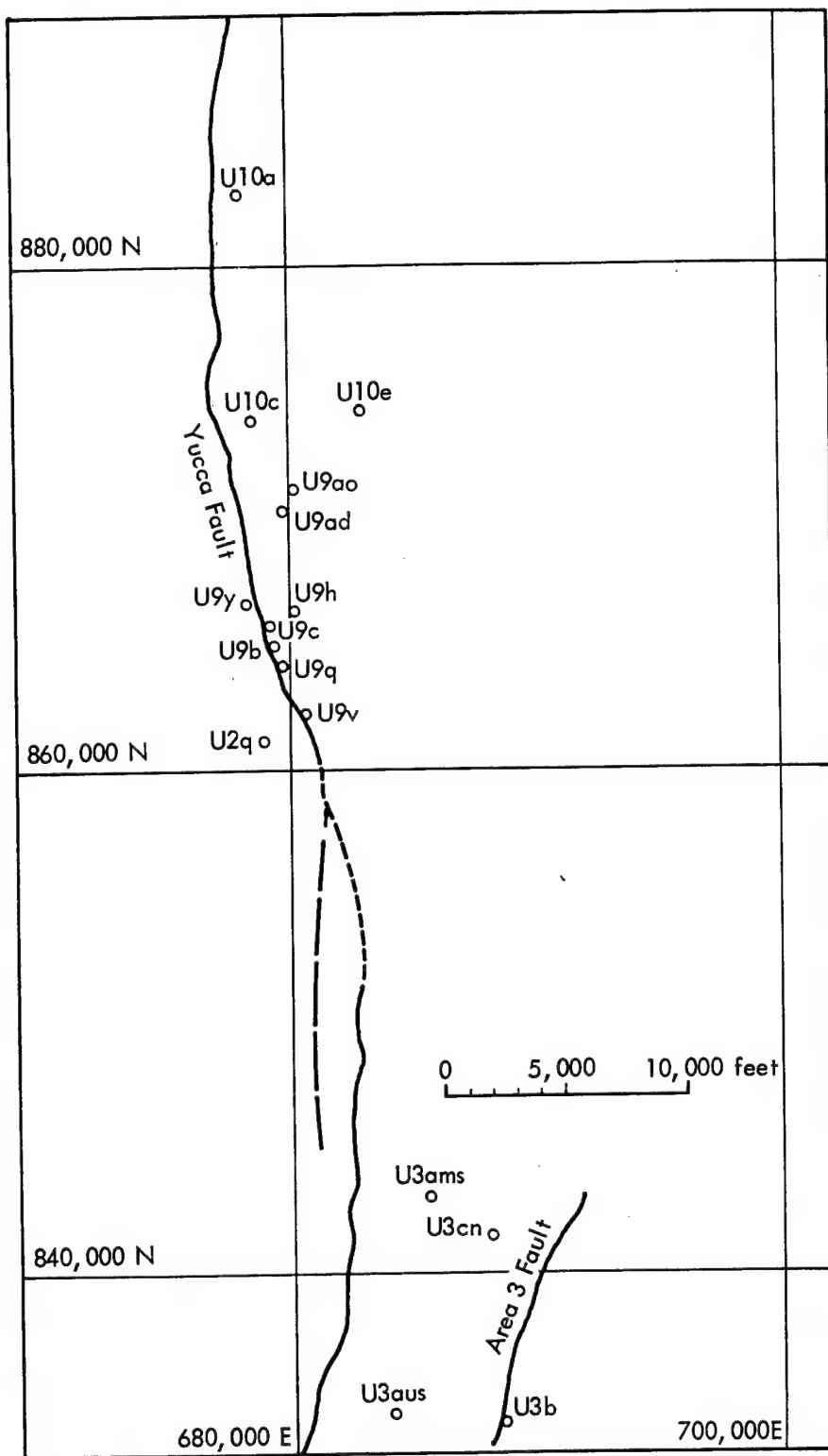
Fig. 33. Yucca Fault and Area 3 Fault and locations of events
that caused known movement along them .

Table IV. Characteristics of 16 events in the vicinity of Yucca Fault and Area 3 Fault (Ref. 22).

Event	Site	Yield (kt)	Contact[a] depth (ft)	Crater dimensions Depth (ft)	Radius (ft)	Volume (10^3 cu. yards)	Collapse time (min)	Remarks
1. Yucca Fault								
Stillwater	U9c	2.8 ± 0.3	1250 A-T	40.0	206	53.4	9.0	No vent; no fault motion
Cimarron	U9h	11.9 ± 0.2	1210 A-T	36.0	259	67.5	44.0	No vent; no fault motion
Aardvark	U3ams	38 ± 0.6	>900 A-T 3000 T-P	73.5	479	641.0	105.2	No vent; 18,000 ft of fracturing along fault, 5 in. vertical displacement
White	U9b	Low	1100 A-T	51.0	243	112.9	12.0	No vent; no fault motion
Haymaker	U3aus	45.5 ± 1.5	>1520 A-T	108.9	461	914.6	24.88	No vent; no fault motion
Sacramento	U9v	Low	>1000 A-T	70.0	225	87.0	6.0	Visible ground heaving
Wichita	U9y	Low	1500 A-T	58.0	222	61.5	5.35	Vented through fissure 50 ft from GZ; no fault motion
Mississippi	U9ad	Low-intermediate	1435 A-T 3250 T-P	125.0	444	815.7	67.5	No fault motion
Bilby	U3cn	~200	850 A-T 2700 T-P	85.6	728	2061	31.0	No vent; 15,000 ft of fracturing along fault; 4 in. vertical displacement; surface heaved ~150 in.
Roanoke	U9q	Low	>1000 A-T	5.0	47.9	0.68	15.0	Seepage around cables; no fault motion
Fore	U9ao	Low-intermediate	1380 A-T 3050 T-P	125.0	463	1451	128.0	No vent; fault motion 3 in. vertical
Klickitat	U10e	Low-intermediate	555 A-T 1950 T-P	122.8	467.5	11.51	78.2	No vent; fault motion
Dub	U10a	Low	1130 A-T	97.0	87.4	83.3	51.0	Fault motion; vertical walls in crater
Turf	U10c	Low-intermediate	1710 A-T	93.0	560	1180	680.0	No vent; fault motion 12 in. vertical
Crepe	U2q	Low-intermediate	1100 A-T 3300 T-P	64.6	350	304	125.0	2 in. vertical motion
2. Area 3 Fault								
Bandicoot	U3bj	Low	1500 A-T	124.5	301	374	5.17	Vented through fissure; small vertical motion
Bilby	U3cn	~200	850 A-T 2700 T-P	85.6	728	2061	31.0	Surface heaved ~150 in.; vertical displacement ~6 in.; 9,000 ft of fracturing along fault

[a] A-T indicates the contact between alluvium and tuff. T-P indicates the contact between tuff and paleozoic rock.

-41-

probably due to gas acceleration, was observed on two events, Sacramento and Bilby. While only one of the nine events showing fault motion vented, there were two out of the total of 16 events that showed dynamic venting associated with ground fissures which apparently intersected surface ground zero, the emplacement hole, or the working point. In addition, one event showed late-time seepage.

Commodore Event

In order to determine the time sequence of motion of the Yucca Fault relative to the detonation of a nuclear explosive, a photographic study of fracturing was conducted as part of the Commodore Event (Ref. 22). The significant results of this study are summarized below:

1. Yucca Fault ruptured at about the time of arrival of the first seismic wave, 0.564 sec after detonation. Fault motion lasted for 0.056 sec.

2. Ground motion caused by the seismic wave lasted for about 3 sec. Two distinct phases were associated with this motion. The first, lasting 0.5 sec, had a relative amplitude of vertical displacement of 2 in. The second, lasting for approximately 2.35 sec, had a similar displacement of 11 in.

3. Fracturing around ground zero was strongly oriented to the northeast and originated about 800 ft southeast of ground zero.

4. Radial and concentric fractures were not evident before the collapse over the explosion point.

Agile Event

As of May 27, 1967, the only documented motion on the Yucca Fault occurred in the Agile Event. Here the explosion caused motion on the Yucca Fault as far as 500 ft northeast and 6000 ft southeast of the site (U2v). The maximum vertical displacement was 0.3 ft.

East Branch of Area 3 Fault and Area 7 Fault

Other sensitive faults in Yucca Flat are the east branch of Area 3 Fault and the Area 7 Fault. The latter, and the two fracture zones west of site U4c,[*] may be classified as sensitive only on the basis of motion caused by explosions. Evidence for movement in recent geologic history is lacking.

PAHUTE MESA FAULTS

The Pahute Mesa area has a thick cover of relatively flat-lying Tertiary volcanic rocks which are locally disturbed by small rhyolite intrusives and cut by numerous northward-trending high-angle faults (Ref. 23). The cross section in Fig. 34 is a few miles north and northeast of the Timber Mountain caldera, and the west end of the cross section extends into the Silent Canyon caldera, where the

---

[*]The Zaza Event in site U4c generated two linear-fracture zones 2000 and 2800 ft west of ground zero in addition to the normal fractures expected around ground zero. The significance of these two sets of fractures is that they continue for thousands of feet, far beyond what is normally expected in Yucca Flat. Thus it has been inferred that they represent buried faults.
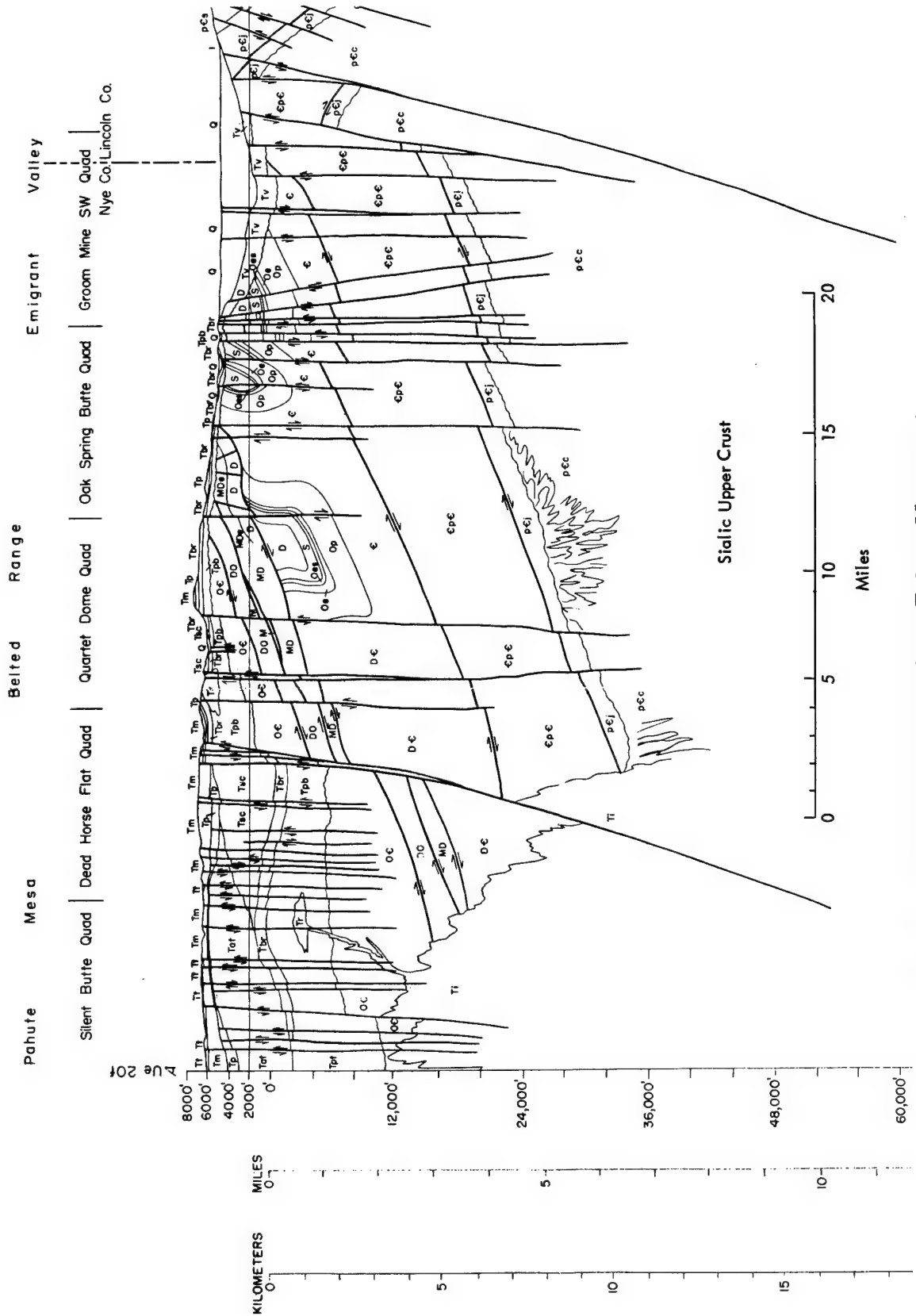
Fig. 34.   Geological section from Pahute Mesa east.

-43-

volcanic sequence is much thicker than to the east.

The Tertiary rocks are assumed to overlie a series of thrust plates composed of uppermost pre-Cambrian to middle Paleozoic sediments which, in turn, unconformably overlie the Precambrian basement complex. The thrust sequence, for the most part, has been projected northwestward from the Yucca Flat area. The Paleozoic rocks are folded where they are exposed at the south end of the Belted Range, and the rock comprising the thrust plates at depth are presumed to be moderately to strongly folded. A general west dip is projected for the thrust plates and assumed for the top of the pre-Cambrian complex. By analogy with other caldera, the Silent Canyon caldera may be underlain by a granite intrusion of similar age.

The fractures resulting from nuclear explosions in Pahute Mesa have been recently reviewed (Ref. 20). Most of the fractures opened by the explosives are on or near previously mapped faults. In most instances, the displacements along the explosion-produced fractures are in the same direction as those in the original structures. In some instances, explosion-produced fractures were opened by subsequent explosions. Lateral movement on some of the fractures indicates that a horizontal component of stress is present in the mesa.

The following description is an example of a typical interaction between a nuclear explosion and the Pahute Mesa stratigraphy.

"An intermediate yield explosion at the U19as site . . . formed numerous small fractures along the cableway, roads and other ground compacted by man. Fluffed ground and overturned stones were seen as far as 2,000 feet from GZ. Thirteen hundred feet northwest of ground zero is a fracture about 1,500 feet long which was opened by the U20g explosion and reopened by the U19as explosion. Maximum displacement was 2 inches down on the northwest. Twenty-five hundred feet farther northwest are three other fractures opened by the U20g event and reopened by the U19as explosion. The only other significant fractures caused by the U19as explosion developed in a northeast-trending zone about 5,000 feet long that passes just east of ground zero." (Ref. 20).

CONCLUSIONS

From these observations and other studies, we draw the following conclusions:

1. Yucca Fault is more sensitive than the Area 3 Fault, and movement along these faults is not systematic.

2. Yucca Fault motion has occurred most often at scaled distances up to $1000 \ W^{1/3}$ ft, Area 3 Fault at distances of up to $500 \ W^{1/3}$ ft.

3. Pahute Mesa motion is associated with pre-existing structural discontinuities. The general linear alignment of the extensively long cracks indicates motion on faults which may extend to considerable depths. The likelihood of venting on Pahute Mesa faults is probably of the same order of magnitude as venting on the faults in Yucca Flat, with which LRL and LASL have had their most extensive experience.

Our current thinking is that faults intersected by expanding cavities are not significant vent paths by the nature of the phenomenology of cavity growth. As soon as the shock vaporizes and melts the rock surrounding the explosive, a liquid seal under megabar pressures closes of the rock from the expanding cavity. Faults or joints which may have extended into the cavity, or lie adjacent to or a short distance from the explosion, are closed as the shock wave moves through the rock and remain closed as the cavity begins to expand into the rock. The "crack" that was part of the fault or joint no longer exists as a crack but rather as a tightly sealed fracture indistinguishable from the rock surrounding it. In some instances, as the rock outside of the cavity begins to unload, pre-existing cracks will begin to open. These cracks will progress back toward the cavity wall, which is now covered with a film of liquid. They may indeed progress through the elastic region, through the plastically deformed region, and into the recrystallized zone, and then open into the liquid-melt coating on the cavity wall. Under these circumstances, with the pressure in the cavity greater than the pressure in the crack, melt will be injected into pre-existing cracks or into some randomly generated crack.

It is conceded, therefore, that under certain geologic geometries pre-existing cracks may act as potential sites for deposition of liquid melt. This phenomenon occurs near or at the end of cavity growth, and the crack paths act as surfaces upon which to quench the melt, condense the more refractory materials, and trap the volatiles. This phenomenon, which has been observed in different experiments, is illustrated in Fig. 35. Injected melt may extend as far as one or two cavity radii into the rock, and then progress no farther. On the other hand, if an expanding cavity is coupled into a poorly stemmed emplacement hole or instrument hole, then the large-diameter hole may offer no resistance to the expanding cavity and may indeed permit venting to occur. In particular, if a hole is only partially stemmed and is intersected some distance above the working point by a joint or fault, then the combination of poor stemming and the presence of a fault or crack can afford a venting path to the material coming from the expanding cavity.

Our policy is to stem all emplacement holes and satellite holes adequately and carefully. Further, it is our policy to avoid emplacement on or immediately adjacent to known faults. We feel, however, that faults adjacent to the device are not important vent paths. Faults intersecting poorly stemmed holes may act as vent paths.

Fig. 35. Wall of a tunnel dug into the vicinity of the cavity of an underground nuclear explosion. The dark areas (arrows) are injected melt that has been quenched in cracks within cold country rock.

Acknowledgments

References

1. J. T. Cherry and W. R. Hurdlow, "Numerical Simulation of Seismic Disturbances," Geophysics 31, 33 (1966).

2. G. Maenchen and S. Sack, The TENSOR Code, Lawrence Radiation Laboratory, Livermore, Rept. UCRL-7316 (1963).

3. J. T. Cherry, "Computer Calculations of Explosion-Produced Craters," Int. J. Rock Mech. Min. Sci. 4, 1 (1967).

4. T. R. Butkovitch, The Gas Equation of State for Natural Materials, Lawrence Radiation Laboratory, Livermore, Rept. UCRL-14729 (1967).

5. E. G. Rapp, Lawrence Radiation Laboratory, Livermore, private communication.

6. J. T. Cherry, D. B. Larson, and E. G. Rapp, A Unique Description of the Failure of a Brittle Material, Lawrence Radiation Laboratory, Livermore, Rept. UCRL-70617 (1967).

7. J. G. Ramsay, Folding and Fracturing of Rocks, (McGraw-Hill, New York, 1967).

8. J. T. Cherry and E. G. Rapp, Calculation of Free-Field Motion for the Piledriver Event, Lawrence Radiation Laboratory, Livermore, Rept. UCRL-50373 (1968).

9. C. R. Boardman, Results of an Exploration into the Top of the Piledriver Chimney, Lawrence Radiation Laboratory, Livermore, Rept. UCRL-50385 (1967).

10. J. Schlocker, Petrology and Minerology of Tatum Salt Dome, Lamar County, Mississippi, U. S. Department of the Interior, Technical Letter Dribble-28 (1963).

11. L. A. Rogers, "Free-Field Motion Near a Nuclear Explosion in Salt: Project Salmon," J. Geophys. Res. 71, 3415 (1966).

12. R. L. Braun, J. S. Kahn, and S. Weissmann, X-Ray Diffraction Analysis of Plastic Deformation in the Salmon Event, Lawrence Radiation Laboratory, Livermore, Rept. UCRL-71249 (1968).

13. J. T. Cherry, D. B. Larson, and E. G. Rapp, Computer Calculations of the Gasbuggy Event, Lawrence Radiation Laboratory, Livermore, Rept. UCRL-50419 (1968).

14. J. A. Korver and D. E. Rawson, Gasbuggy Postshot Investigations in GB-ER, Lawrence Radiation Laboratory, Livermore, Rept. UCRL-50425 (1968).

15. C. E. Chapin, Lawrence Radiation Laboratory, Livermore, private communication (1968).

16. A. L. Edwards, TRUMP: A Computer Program for Transient and Steady State Temperature Distributions in Multidimensional Systems, Lawrence Radiation Laboratory, Livermore, Rept. UCRL-14754 Rev. 1 (1968).

17. C. W. Olsen, "Time History of the Cavity Pressure and Temperature Following a Nuclear Detonation in Alluvium," J. Geophys. Res. 72, 5037 (1967).

18. H. Rodean, Lawrence Radiation Laboratory, Livermore, private communication.

19. F. W. Aron, Lawrence Radiation Laboratory, Livermore, private communication.

20. D. D. Dickey and W. L. Ellis, <u>Principle Linear Fractures Resulting from Nuclear Explosions in Pahute Mesa,</u> U. S. Geological Survey, Tech. Letter, Special Studies 67 (1968).

21. D. D. Dickey, U. S. Geological Survey, private communication.

22. F. A. McKeown, D. D. Dickey, and W. L. Ellis, <u>Maps and Classification of Explosion-Produced Fractures in Yucca Flat,</u> U. S. Geological Survey, Tech. Letter NTS-195 Supp. 1 (1967).

23. P. J. Barosh, <u>Preliminary Geologic Section from Pahute Mesa, Nevada Test Site, to Enterprise, Utah,</u> U. S. Geological Survey, Tech. Letter, Interagency Rept. NTS-1 (1967) (OUO).

Distribution

GS/dh